

1 Lateral variations in lower crustal strength control the  
2 temporal evolution of mountain ranges: examples from  
3 south-east Tibet

4 Camilla Penney<sup>1\*</sup>, Alex Copley<sup>1</sup>

5 April 15, 2020

6 Key points:

- 7 • Lateral variations in lower crustal strength provide a first-order control on the shape  
8 and temporal evolution of mountain ranges.
- 9 • Strong lower crust in the Sichuan Basin can explain the development of topography in  
10 the Longmen Shan without a lower crustal channel.
- 11 • Lateral transport of samples should be considered in calculating and interpreting  
12 palaeoelevations from stable-isotope palaeoaltimetry.

---

\*Corresponding author: cp451@cam.ac.uk, <sup>1</sup>COMET, Bullard Laboratories, Department of Earth Sciences, University of Cambridge, Cambridge, UK

## 13 **Abstract**

14 Controversy surrounds the rheology of the continental lithosphere, and how it controls the  
15 evolution and behaviour of mountain ranges. In this study, we investigate the effect of lat-  
16 eral contrasts in the strength of the lower crust, such as those between cratonic continental  
17 interiors and weaker rocks in the adjacent deforming regions, on the evolution of topogra-  
18 phy. We combine numerical modelling and recently published results from stable-isotope  
19 palaeoaltimetry in south-east Tibet. Stable-isotope palaeoaltimetry in this region provides  
20 constraints on vertical motions, which are required to distinguish between competing mod-  
21 els for lithosphere rheology and deformation. We use numerical modelling to investigate the  
22 effect of lateral strength contrasts on the shape and temporal evolution of mountain ranges.  
23 In combination with palaeoaltimetry results, our modelling suggests that lateral strength  
24 contrasts provide a first-order control on the evolution of topography in south-east Tibet.  
25 We find that the evolution of topography in the presence of such strength contrasts leads  
26 to laterally-varying topographic gradients, and to key features of the GPS- and earthquake-  
27 derived strain-rate field, without the need for a low-viscosity, lower-crustal channel. We  
28 also find that palaeoaltimetric samples may have been transported laterally for hundreds  
29 of kilometres, an effect which should be accounted for in their interpretation. Our results  
30 are likely to be applicable to the evolution of mountain ranges in general, and provide an  
31 explanation for the spatial correlation between cratonic lowland regions and steep mountain  
32 range-fronts.

## 33 **Plain Language Summary**

34 The rocks which make up the Earth's continents move and change shape in response to  
35 tectonic forces. How rocks respond to these forces depends on their material properties,  
36 and can vary in space and time. These material properties, therefore, control the shape

37 of mountain ranges and how mountains grow. This study investigates why some mountain  
38 ranges have steep fronts, whilst others have gentle gradients. We look at how regions made  
39 up of strong rocks (such as the Sichuan Basin) affect the shape and growth of adjacent  
40 mountain ranges. We find that mountain ranges with steep fronts can form when weaker  
41 rocks move over stronger ones. Recent measurements of oxygen in ancient soils suggests that  
42 parts of the south-eastern margin of the Tibetan Plateau (between the Sichuan Basin and  
43 the Central Lowlands of Myanmar) have been high since about 50 million years ago, and  
44 that the area has risen more slowly than has previously been estimated. In south-east Tibet,  
45 the pattern of earthquakes, and how fast the mountains have grown, can be explained by  
46 these strong areas, without invoking complicated material properties in the mountain ranges.  
47 Such strong regions may be important in controlling the shape of mountain ranges globally.

## 48 **1 Introduction**

49 The strength of the lithosphere provides a first-order control on the distribution of strain  
50 within it. Strength, here, means resistance to deformation, which might be controlled by the  
51 stresses transmitted across faults in the brittle part of the lithosphere or the rheology asso-  
52 ciated with ductile creep in the lower crust and upper mantle. Lateral strength contrasts,  
53 such as those between anhydrous rocks in cratonic continental interiors, from which volatiles  
54 have been removed by previous partial melting, and more hydrous rocks in the adjacent de-  
55 forming regions, are a feature of continental lithosphere globally. Such contrasts control the  
56 distribution of strain in the continents and, therefore, the evolution of mountain ranges (e.g.  
57 Vilotte et al., 1984; England and Houseman, 1985; Flesch et al., 2001; Jackson et al., 2008).  
58 Regions with strong crust, such as cratons, tend to accommodate little strain in comparison  
59 to their surroundings. In the India–Eurasia collision, for example, the accreted terranes  
60 which form the southern margin of Eurasia, rather than cratonic India, have accommodated

61 most of the shortening. Here we investigate the effect of lateral contrasts in the strength of  
62 the lower crust on the temporal evolution of mountain belts.

63

64 A key outstanding question about the effect of lateral strength contrasts is how regions  
65 with strong lower crust, and the flow of less viscous material over and around them, affect the  
66 evolution of mountain ranges over tens of millions of years. Previous studies of continental  
67 deformation demonstrate that models which are able to reproduce instantaneous strain rates  
68 do not necessarily lead to the formation of the observed topography over time (e.g. Houseman  
69 and England, 1986; England and Houseman, 1986), so incorporating temporal evolution is  
70 an important extension to models considering the geologically-instantaneous effects of such  
71 contrasts (e.g. Copley, 2008; Bischoff and Flesch, 2019). Our interest is in understanding the  
72 physical controls on mountain building, and the constraints which recently-published stable-  
73 isotope palaeoaltimetry observations can provide on lithosphere rheology. Vertical motions,  
74 to which palaeoaltimetry observations are sensitive, have the potential to distinguish be-  
75 tween rheological models which lead to the same horizontal surface velocities (Copley, 2008;  
76 Flesch et al., 2018). Understanding the implications of these observations, and the associ-  
77 ated caveats is, therefore, critical to constraining lithosphere rheology. Numerical models  
78 with a small number of parameters allow us to test whether lower-crustal strength contrasts,  
79 consistent with observations, can reproduce variations in topographic gradients, or whether  
80 other driving mechanisms are required. In this study, we combine new palaeoaltimetry ob-  
81 servations from south-east Tibet, with a simple 3D model of crustal deformation, to explore  
82 the effects of lateral strength contrasts in controlling continental deformation.

83

84 The south-eastern margin of the Tibetan plateau (south-east Tibet, Figure 1) is a good  
85 place to study the effect of lateral strength contrasts. Low elevations, relief and strain rates  
86 (both seismic – Figure 1 – and geodetic – Zheng et al., 2017; Maurin et al., 2010) in the

87 Sichuan Basin and the Central Lowlands of Myanmar suggest that these regions experience  
88 relatively little deformation. These regions are, therefore, likely to be strong in comparison  
89 to the high region between them, and the mountain belts which surround them, which have  
90 undergone significant recent and cumulative deformation. The Sichuan Basin is covered  
91 by  $\sim 10$  km of sediments (Hubbard and Shaw, 2009), underlain by Paleoproterozoic crust  
92 (Burchfiel et al., 1995) with high seismic velocities in the upper mantle (e.g. Lebedev and  
93 Nolet, 2003; Li and Van Der Hilst, 2010). Post-seismic motion after the 2008 Wenchuan  
94 earthquake suggests a strength contrast across the Longmen Shan (Huang et al., 2014), as  
95 do differences in elastic thickness between the Longmen Shan and the Sichuan Basin derived  
96 from gravity anomalies (Fielding and McKenzie, 2012).

97

98 Although the Central Lowlands of Myanmar have been less extensively studied than the  
99 Longmen Shan, the lack of topography, and the presence of undeformed Miocene sediments  
100 suggest low rates of post-Miocene deformation (Wang et al., 2014). Initial GPS measure-  
101 ments by Maurin et al. (2010) suggest that central Myanmar, west of the Sagaing fault,  
102 deforms in a coherent manner. Earthquakes in the Central Lowlands of Myanmar, shown in  
103 Figure 1b, are associated either with strike-slip motion on the Sagaing fault, on the eastern  
104 margin of the lowlands (which accommodates a component of the oblique India–Eurasia con-  
105 vergence; Maurin et al., 2010) or with active subduction beneath the Indo-Burman ranges  
106 (e.g. Stork et al., 2008; Steckler et al., 2016, yellow focal mechanisms in Figure 1b have  
107 depths  $> 50$  km). The seismic strain rate within the Central Lowlands is, therefore, low, at  
108 least in the instrumental period.

109

110 In contrast, the high regions of south-east Tibet deform rapidly, with kinematics de-  
111 scribed in detail by Copley (2008), who also summarised the work of previous authors. Since  
112 that study, numerous thrust-faulting earthquakes have occurred along the Longmen Shan,

113 including the 2008 Wenchuan and 2013 Lushan earthquakes and their aftershocks (Figure 1).  
114 These earthquakes, and subsequent analysis of shortening on structures imaged in seismic  
115 profiles (Hubbard and Shaw, 2009), demonstrate that active shortening of the brittle upper  
116 crust is occurring across the Longmen Shan.

117

118 Much of the morphology of south-east Tibet is dominated by deeply-incised river valleys,  
119 often following the traces of strike-slip faults (Wang and Burchfiel, 1997). Collectively these  
120 strike-slip faults accommodate south-eastwards motion of high topography relative to both  
121 the Sichuan Basin and the Central Lowlands of Myanmar (e.g. Shen et al., 2005), with the  
122 faults on opposite sides of the high region accommodating opposite senses of shear (Fig-  
123 ure 1a). The Xianshuihe and Sagaing faults (Figure 1a) have left- and right-lateral geodetic  
124 slip rates of  $\sim 7\text{--}9\text{ mm yr}^{-1}$  and  $\sim 18\text{ mm yr}^{-1}$  respectively (Zheng et al., 2017; Maurin et al.,  
125 2010). The region of distributed left-lateral faulting east of the Sagaing fault (Figure 1a)  
126 accommodates right-lateral shear on north-south striking planes through rotations about  
127 vertical axes (Copley, 2008).

128

129 A suite of models (e.g. Royden et al., 1997; Clark and Royden, 2000; Clark et al., 2005a)  
130 have focussed on the possibility of a low viscosity, lower-crustal channel producing the steep  
131 topography of the Longmen Shan, and the gentle topographic gradients to the south of the  
132 basin. By extending these channel flow models to include rigid regions, Cook and Royden  
133 (2008) argued for the importance of both a strong Sichuan Basin and flow in a mid/lower  
134 crustal channel, in the formation of steep topography across the Longmen Shan. Chen et al.  
135 (2013a) and Chen et al. (2013b) used 2D thermo-mechanical models with extrapolated lab-  
136 oratory flow laws to demonstrate that the craton was an important control on deformation  
137 in the region. We build up on this work by using a simple 3D model to isolate the effects  
138 of this rigid, cratonic region, and comparing the results to observational constraints from

139 palaeoaltimetry.

140

141 Vertical velocities can distinguish between competing models of depth-dependent rheol-  
142 ogy which would lead to the same horizontal velocities (Copley, 2008; Flesch et al., 2018;  
143 Bischoff and Flesch, 2019). Copley (2008) demonstrated that rapid flow at depth associated  
144 with a weak mid-to-lower crust would lead to faster instantaneous vertical motions than  
145 coherent upper- and lower- crustal deformation. The specific rates were based on instanta-  
146 neous calculations, so would not necessarily apply to the geologically-recorded uplift rates,  
147 but exemplify the possibility of using vertical motions to distinguish between different mod-  
148 els of depth-dependent rheology.

149

150 Previous quantitative studies of topographic evolution in south-east Tibet have focussed  
151 on thermochronology (e.g. Kirby et al., 2002; Clark et al., 2004; Wang et al., 2012, 2016).  
152 Thermochronometric ages give information about exhumation, which is controlled by the in-  
153 terplay between tectonics and erosion. Such ages have been interpreted to imply that rapid  
154 uplift occurred  $\sim 13\text{--}5$  Ma, based on the identification of geomorphic surfaces presumed to  
155 have formed at low elevation (Clark et al., 2005a, 2006). However, it has been suggested  
156 that such low-relief, erosional surfaces can also form at high elevations (e.g. Liu-Zeng et al.,  
157 2008; Yang et al., 2015) and that increased exhumation may have been related to changes in  
158 the base level of rivers draining the region (e.g. Richardson et al., 2008). The interpretation  
159 of the existing thermochronometric data in terms of elevation history is therefore unclear. In  
160 this study we make use of new estimates of palaeoelevation from stable-isotope geochemistry,  
161 which provide an opportunity to quantitatively constrain the elevation history of south-east  
162 Tibet and, therefore, to distinguish between competing models of lithosphere rheology and  
163 mountain-range evolution.

164

165 We first summarise recently published results from stable-isotope palaeoaltimetry (Sec-  
166 tion 2) to constrain the uplift and elevation history of south-east Tibet. We then use fluid-  
167 dynamical modelling of the mountain range (described in Section 3) to investigate the effects  
168 of lateral strength contrasts on the evolution of topography through time, and compare our  
169 results to south-east Tibet (Section 4).

170

171 Although the results presented here are in the context of South East Tibet, the presence  
172 of lateral strength contrasts is a common feature of mountain ranges globally (e.g. Lamb,  
173 2000; Jackson et al., 2008; Nissen et al., 2011). In particular, many mountain ranges, both  
174 active and older, have edges adjacent to cratons (McKenzie and Priestley, 2008). – regions  
175 of (often thick) continental lithosphere, usually composed of Proterozoic or Archean crust,  
176 which have remained relatively undeformed through multiple deformation cycles (Holmes,  
177 1965). In section 5, therefore, we discuss that applicability of our results to the temporal  
178 evolution of mountain ranges in general.

179

## 180 **2 Palaeoaltimetry**

181 Stable-isotope palaeoaltimetry uses systematic variations in the isotopic composition of pre-  
182 cipitation with elevation to derive the palaeoelevation of sample sites (e.g. Rowley et al.,  
183 2001). These techniques have been developed in order to place quantitative constraints on  
184 the elevation history of orogenies, such as Tibet, but they have not yet been extensively  
185 used as a constraint in dynamic models. South-east Tibet is a good region to carry out  
186 palaeoaltimetry studies. Moisture paths from the ocean to high topography in the region are  
187 simple, as the Rayleigh fractionation relationship between the oxygen-isotope composition  
188 of precipitation and elevation in present-day elevation transects shows (Hren et al., 2009).

189

190 Figure 2 shows results from six recent palaeoaltimetry studies in south-east Tibet, which  
191 use soil-deposited (Hoke et al., 2014; Xu et al., 2016; Tang et al., 2017; Gourbet et al., 2017) or  
192 lacustrine (Li et al., 2015; Xu et al., 2016; Gourbet et al., 2017; Wu et al., 2018) carbonates to  
193 derive the oxygen-isotope composition of palaeo-precipitation and, hence, palaeoelevations.  
194 In south-east Tibet, particularly in the Jianchuan Basin (Figure 1a), the age of sampled for-  
195 mations is a significant source of uncertainty (Hoke, 2018). Gourbet et al. (2017) revised the  
196 age of formations previously mapped as Miocene, and mid-Eocene, to the late Eocene, based  
197 on more precise dating (Figure 2b). As well as the direct uncertainty as to when a sample was  
198 deposited, hotter global temperatures in the Eocene (Savin, 1977; Miller et al., 1987; Zachos  
199 et al., 2001) alter the relationship between isotopic composition and elevation, resulting in  
200 different paleoelevation estimates (filled and unfilled symbols in Figure 2b show paleoeleva-  
201 tion estimates calculated using modern and Eocene relationships respectively). However, the  
202 differences in palaeoelevation resulting from these hotter temperatures are generally much  
203 less than the kilometre scale of interest for dynamic modelling, even for upper-bound esti-  
204 mates of Eocene temperature (region 4, Figure 2b Hoke et al., 2014; Li et al., 2015; Tang  
205 et al., 2017; Wu et al., 2018).

206

207  $\delta^{18}O$  at sea level is also time-dependent. Licht et al. (2014) found very negative values of  
208  $\delta^{18}O$  in an Eocene gastropod and rhinoceroid from Myanmar, taken as sea level references for  
209 the time. Preliminary results from isotopic analysis of soil-deposited carbonates in the same  
210 area show similarly low  $\delta^{18}O$  (Licht et al., 2019). A more negative starting value leads to  
211 lower palaeoelevation estimates, since Rayleigh fractionation predicts increasingly negative  
212  $\delta^{18}O$  with elevation. These improved estimates of starting composition, as well as the dating  
213 discussed above, have led to recalculations of palaeoelevation in south-east Tibet (Gourbet  
214 et al., 2017; Wu et al., 2018, shown as dark-outlined symbols in Figure 2b, the original es-

215 timates are shown with pale outlines), and we use these in our uplift rate calculations in  
216 preference to the original studies.

217

218 Uplift rates can be derived from stable-isotope palaeoaltimetry if samples can be taken  
219 from rocks of multiple ages at the same location. These rates, therefore, only reflect points  
220 in space and time which are preserved in the carbonate record. Where such rates can be  
221 inferred they are shown in Figure 2b. All of these inferred uplift rates are  $<0.3\text{mm yr}^{-1}$ .

222

223 In all the regions shown in Figure 2, except regions 5 and 6, which are the furthest to the  
224 south-east, paleoelevations similar present-day elevations are found in the oldest sampled  
225 formations. To the north-west (region 1), Tang et al. (2017) suggest that topography may  
226 have been high since before the Eocene. Although Xu et al. (2016)'s measurements have  
227 significant uncertainty in the moisture source, they suggest a lower bound for the elevation  
228 of the Longmen Shan of  $\sim 3000$  m, compared to present-day elevations of 2800-3700 m, in  
229 the late Miocene. To the south-east, region 5 may have experienced some uplift since the  
230 late Miocene, at rates  $<0.3\text{ mm yr}^{-1}$ , and region 6 was likely at its present elevation by the  
231 late Miocene.

232

233 These stable-isotope palaeoaltimetry results suggest that at least some areas of present-  
234 day south-east Tibet have been high since the late Eocene, and are likely to have reached  
235 present-day elevations prior to the onset of rapid exhumation inferred by Clark et al. (2005b)  
236 from the incision of river gorges (gray region in Figure 2b). Uplift rates across south-east  
237 Tibet are likely to have been much lower ( $<0.3\text{ mm yr}^{-1}$ ) than would be predicted if all the  
238 uplift in the region had occurred since the late Miocene. Recently published thermochronol-  
239 ogy is also consistent with this palaeoaltimetric data, suggesting that topography across the  
240 Longmenshan had begun to develop by the Oligocene (Wang et al., 2012), and that uplift

241 may have been ongoing since the Paleocene (Liu-Zeng et al., 2018).

242

## 243 **3 Dynamical modelling**

244 In tandem with the published palaeoaltimetry estimates summarised in section 2, we use  
245 numerical modelling to investigate the effect of lateral contrasts in lower crustal strength  
246 on the temporal evolution of mountain ranges. We first summarise the work of previous  
247 authors (section 3.1) and then describe the setup for the model used here (section 3.2) and  
248 our boundary conditions (section 3.3), before describing the model results in section 4. We  
249 emphasise that our model is intended to investigate the first-order effects of lateral strength  
250 contrasts on the multi-million-year development of long-wavelength topography in general,  
251 rather than to simulate the detailed evolution of south-east Tibet.

252

### 253 **3.1 Previous Models**

254 In regions of distributed deformation, the continental lithosphere can be modelled as a con-  
255 tinuum (commonly a viscous fluid), with motion driven by horizontal pressure gradients  
256 – resulting from gravity acting on elevation contrasts – and by the relative motion of the  
257 bounding plates (e.g. England and McKenzie, 1982, 1983; Houseman and England, 1986;  
258 Royden et al., 1997; Lamb, 2000; Flesch et al., 2001; Reynolds et al., 2015; Flesch et al.,  
259 2018). Many authors use the thin-viscous-sheet model, which assumes negligible depth vari-  
260 ations in horizontal velocities (England and McKenzie, 1982, 1983). This model implicitly  
261 assumes that the top and base of the lithosphere experience shear tractions which are small  
262 in comparison to other components of the deviatoric stress tensor (here referred to as a stress-  
263 free boundary condition, after McKenzie et al., 2000). In the model, this corresponds to flow

264 over a less viscous fluid (the asthenosphere). Such models can only produce steep-fronted  
265 topography if the lithosphere has an effective power-law rheology with a high stress exponent  
266 (typically greater than 3, i.e. shear-thinning, e.g. Houseman and England, 1986; Lechmann  
267 et al., 2011). The typical gradients in these models are still much less steep than those in  
268 steep-fronted mountain ranges such as the Himalayas and the Longmen Shan (England and  
269 Houseman, 1986). Geologically, stress exponents greater than 1 are associated with rocks  
270 deforming by dislocation creep (e.g. Stocker and Ashby, 1973).

271

272       Steep topographic gradients often occur adjacent to lateral contrasts in lithosphere strength.  
273 Such regions are commonly associated with large gradients in crustal thickness, and, if less  
274 viscous material flows over a higher viscosity region, this is equivalent to flow over a rigid  
275 base (defined as zero-horizontal velocity, or no-slip, after McKenzie et al., 2000). In such  
276 regions the thin-viscous sheet approximation breaks down, because flow over a rigid base is  
277 accommodated by vertical gradients of horizontal velocity in the flowing layer. Medvedev  
278 and Podladchikov (1999a) presented an extension to the thin-viscous sheet model to allow  
279 for rapid spatial variations in material properties, which was applied to 2D geodynamic  
280 scenarios by Medvedev and Podladchikov (1999b). An alternative approach is to use full  
281 thermo-mechanical models in either 2D (e.g. Beaumont et al., 2001) or 3D (e.g. Lechmann  
282 et al., 2011; Pusok and Kaus, 2015). Here we discuss a simplified approach, which allows us  
283 to incorporate flow over both stress-free and rigid boundaries into a single 3D model with a  
284 small number of adjustable parameters.

285

286       Previous studies incorporating vertical gradients of horizontal velocity have focused on  
287 reproducing geologically-instantaneous deformation in south-east Tibet (e.g. Copley, 2008;  
288 Lechmann et al., 2014; Bischoff and Flesch, 2019). These studies have demonstrated that key  
289 features of the instantaneous earthquake- and GPS-derived velocity field can be explained

290 by lateral viscosity contrasts between cratonic blocks and the surrounding mountain ranges.  
291 Studies which have investigate the effects of these cratonic blocks on the temporal evolution  
292 of topography in south-east Tibet have used complex models at the scale of entire collision  
293 zones (e.g. Pusok and Kaus, 2015), or imposed external forcing or velocities to drive the  
294 flow (e.g. Cook and Royden, 2008). Here, we use a simple model of 3D crustal deformation,  
295 described below, to isolate the effects of lateral strength contrasts on the evolution of topog-  
296 raphy through time. Our interest is in understanding the physical controls on topographic  
297 evolution, in particular the development of contrasting topographic gradients. Consideration  
298 of the time-evolution of the topography is important because it allows us to investigate the  
299 constraints which can be provided by newly-available palaeoaltimetry data.

300

## 301 **3.2 Model Setup**

302 We model the lithosphere as a viscous fluid. The geometry and boundary conditions we  
303 use are based on the long-wavelength topography of south-east Tibet (Figure 3). Using a  
304 geometry similar to south-east Tibet allows us to make use of the palaeoaltimetric results  
305 described in Section 2 in assessing the uplift rates associated with the model.

306

307 GPS velocities relative to Eurasia in south-east Tibet are sub-parallel to topographic  
308 gradients (Figure 3). Movement of material along topographic gradients suggests that the  
309 deformation in south-east Tibet is influenced by gravitational potential energy contrasts.  
310 The models we investigate here, therefore, include gravitational potential energy as a driv-  
311 ing force; deformation in these models is driven by gravity acting on crustal thickness con-  
312 trasts, without applied compressive forces or imposed boundary velocities. This category  
313 of models has been described by Lechmann et al. (2014) as “density driven”. Analogous  
314 models have been applied since the 1980s to the gravitational spreading of crustal thrust

315 sheets (e.g. Ramberg, 1981; Merle and Guillier, 1989). Here we consider deformation on  
316 the lithosphere scale, rather than the lengthscale of individual thrust sheets. These studies  
317 also considered analogues between glaciological and geological gravity-driven deformation,  
318 including the possibility of both stress-free and no-slip basal boundary conditions (Ramberg,  
319 1981). We extend this analogy here by using methods from ice-sheet modelling to solve the  
320 governing equations.

321

322 We solve the Stokes' equations using the method proposed by Pattyn (2003), which  
323 includes vertical gradients of horizontal velocities (Appendix A). This method allows us  
324 to model flow over a stress-free base and also a rigid base, representing regions of strong  
325 lower crust, as suggested by Medvedev and Podladchikov (1999a), unlike the original thin-  
326 viscous-sheet model (England and McKenzie, 1982, 1983). Our method neglects horizontal  
327 derivatives of vertical velocities, which are expected to become important immediately ad-  
328 jacent to the change in basal boundary condition (Schmalholz et al., 2014). Pattyn (2003)  
329 demonstrated that the effect of these gradients being large is confined to a region over similar  
330 lateral extent to the thickness of the deforming layer (1–2 grid cells in our model), and that  
331 this does not affect the overall behaviour of the model.

332

333 The method we use here has previously been used to calculate instantaneous strain rates  
334 in south-east Tibet (Copley, 2008). Reynolds et al. (2015) extended this approach to model  
335 the temporal evolution of the Sulaiman Ranges by re-writing the incompressibility condi-  
336 tion as a diffusion equation for topography (Pattyn, 2003). We use an improved method  
337 (described in detail in Appendix A) to solve this diffusion equation, calculating diffusivi-  
338 ties on a staggered grid, and using the generalised minimum residual method (Saad and  
339 Schultz, 1986) to solve the resulting sparse matrix equations. We use a regular horizontal  
340 grid of 15 km×15 km, and 20 grid points in the vertical, which are re-scaled at each time step

341 (Appendix A; Pattyn, 2003). The assumptions and set-up of this model are discussed below.

342

343 We model the deforming crust as an isoviscous, Newtonian fluid. Using a simple rheology  
344 allows us to test the extent to which topographic evolution in south-east Tibet is controlled  
345 by the presence of lateral lower crustal strength contrasts, and whether additional rheological  
346 complexity is required to explain the geophysical and geological observations. The simple  
347 rheology we use contrasts with the approach of previous authors studying the effect of a  
348 strong craton on the evolution of topography in south-east Tibet. For example, Chen et al.  
349 (2013a) used a 2D model with multiple rock types and an assumed geotherm. Cook and  
350 Royden (2008) included a weak lower crustal channel and drove deformation within their  
351 model through an imposed velocity at its base. By using a simpler rheology, we are able  
352 to isolate the effects of lower crustal strength contrasts on the evolution of topography. We  
353 discuss the possible effects of a more complicated rheology in Section 5. The velocity of  
354 the fluid is linearly dependent on the choice of viscosity, so although we use a viscosity of  
355  $10^{22}$  Pas here (as suggested for south-east Tibet by Copley and McKenzie, 2007), the models  
356 can be considered to apply to different viscosities by scaling the time and velocities. For  
357 example, the topography after 50 Myr of model evolution with a viscosity of  $10^{22}$  Pas would  
358 be the same as that after 5 Myr for a viscosity of  $10^{21}$  Pas. The velocities would be 10 times  
359 greater in the  $10^{21}$  Pas case.

360

361 Figure 4 shows a schematic of our model setup. High viscosity regions, analogous to the  
362 lower crust of the Sichuan Basin and the Central Lowlands of Myanmar, are simulated by  
363 setting horizontal velocities to zero in part of the model with a specified thickness (“basal  
364 thickness”, grey areas in Figure 4). Flow can occur over and around these rigid regions  
365 (“basins”, Basin E and Basin W in Figure 4). The basal thickness is equivalent to the thick-  
366 ness of strong lower crust. The Sichuan Basin is connected to the South China craton (e.g.

367 Li and Van Der Hilst, 2010), which provides a resistive force, so the basins in our model  
368 are not advected with the flow. By setting velocities to zero in these basin regions, we are  
369 assuming that the Sichuan Basin and Central Lowlands of Myanmar have behaved rigidly  
370 over the 50 Myr of deformation which we model. This approach is suggested by inferences of  
371 strong lower crust and upper mantle in the Sichuan Basin and Central Lowlands of Myanmar  
372 (Section 1; Li and Van Der Hilst, 2010; Huang et al., 2014). We use crustal thicknesses in the  
373 Longmen Shan and Sichuan Basin of 65 and 36–40 km respectively (e.g. Liu et al., 2014), with  
374 4.5 km of elevation contrast, and a constant crustal density,  $\rho_c = 2700 \text{ kg m}^{-3}$ , to determine  
375 the lower crustal viscosity required for our assumption of rigidity to hold. The buoyancy force  
376 associated with this crustal thickness contrast can be calculated by integrating the pressure  
377 difference between the two columns of crust (e.g. Artyushkov, 1973; Molnar and Tapponnier,  
378 1978; Dalmayrac and Molnar, 1981), giving a maximum buoyancy force of  $7 \times 10^{12} \text{ N m}^{-1}$ .  
379 This buoyancy force results in a maximum normal stress of 200 MPa acting on the Sichuan  
380 Basin. If this topographic contrast has existed since 50 Mya (the effective start time of our  
381 model) then for the Sichuan Basin, which is  $\sim 300 \text{ km}$  wide, to have deformed by less than one  
382 grid cell in our model (15 km), requires a strain rate in the lower crust,  $\dot{\epsilon} \leq 3.2 \times 10^{-17} \text{ s}^{-1}$ .  
383 In this scenario the viscosity of the crust in the Sichuan Basin would need to be greater than  
384  $6 \times 10^{24} \text{ Pas}$  to remain undeformed by buoyancy forces associated with crustal thickness  
385 contrasts. The viscosity required would be lower if the topographic contrast were supported  
386 for a shorter time. We can test whether this viscosity is reasonable using laboratory-derived  
387 flow laws. We use the dry flow laws for typical lower crustal minerals from Bystricky and  
388 Mackwell (2001) and Rybacki et al. (2006), and calculate the temperature corresponding to  
389 a viscosity of  $6 \times 10^{24} \text{ Pas}$  at the Moho (36–40 km Liu et al., 2014), assuming lithostatic  
390 pressure and a grain size of 1 mm. For both flow laws, the viscosity will be  $\geq 6 \times 10^{24} \text{ Pas}$  if  
391 the temperature is less than  $\sim 800\text{--}900^\circ\text{C}$ . Moho temperatures in undefining Precambrian  
392 crust are typically  $\sim 600^\circ\text{C}$  (McKenzie et al., 2005), meaning that the viscosity required

393 for the Sichuan Basin to behave rigidly on the timescales of our model is consistent with  
394 laboratory-derived flows laws. Rather than adding an additional parameter to our model  
395 we therefore model the basin lower crust as rigid. As discussed in section 1, the geological  
396 structure of the Central Myanmar Basin is less well constrained than that of the Sichuan  
397 Basin, but it also acts in a rigid manner, so for simplicity we make the same assumption there.

398

399 Outside the basins, the base of the current is stress-free (England and McKenzie, 1982,  
400 1983; Copley and McKenzie, 2007), implying that the asthenosphere imposes negligible shear  
401 stress on the base of the lithosphere. Since we only model the deformation of the crust, a  
402 further assumption is that the crust and lithospheric mantle deform coherently in the re-  
403 gion with the stress-free base. In this case, vertical planes in the lithosphere will deform by  
404 pure shear. Since the horizontal velocities will not vary with depth, the effect of imposing a  
405 stress-free boundary condition at the base of the crust is the same as imposing this condition  
406 at the base of the lithosphere (because we assume isostatic compensation at the Moho, see  
407 below). Copley (2008) demonstrated the possibility of coherent lower crust and lithospheric  
408 mantle deformation in south-east Tibet with rheologies extrapolated from laboratory flow  
409 laws. Although such extrapolations lead to vertical gradients in viscosity, in many cases  
410 these gradients, and the length-scales over which they occur, are insufficient to result in  
411 appreciable contrasts in horizontal velocities.

412

413 The top surface of the current is stress-free throughout the model domain, representing  
414 the lack of significant tractions imposed by the atmosphere. We track particles on this sur-  
415 face, which move with the horizontal velocity at their location at each time step. These  
416 particles are analogous to the samples used in palaeoaltimetric studies.

417

418 We impose isostatic compensation at the base of the crust relative to a column of mantle

419 (Flesch et al., 2001), with densities of  $2700 \text{ kg m}^{-3}$  and  $3300 \text{ kg m}^{-3}$  respectively. Assum-  
420 ing isostatic compensation neglects flexural support of the topography. By using a viscous  
421 model, we are implicitly considering long-wavelength deformation (motivated by the long-  
422 wavelength shape of the topography in Figure 3). Free-air gravity anomalies from south-east  
423 Tibet suggest that flexure plays a role in supporting the topography on relatively short-  
424 wavelengths ( $\sim 50 \text{ km}$  into the Longmen Shan), which means that isostatic compensation  
425 is an appropriate assumption throughout most of the model domain. At the edge of the  
426 basin region, where flexural support may be important, flexure would be expected to give  
427 a shape for the basal boundary intermediate between full isostatic compensation, which we  
428 use here, and a base which cannot move vertically in response to loading, a case which is  
429 often considered in the fluid dynamics literature (e.g. Huppert, 1982). The implications of  
430 assuming isostatic compensation are discussed in Section 4.

431

432 In some models we investigate the interaction between erosion and propagation of the  
433 current by incorporating an erosive term;

$$\frac{\partial s}{\partial t} = -\kappa |\nabla s|, \quad (1)$$

434 where  $\kappa$  is a constant. Gradient-dependent erosion is suggested by higher erosion rates and  
435 greater cumulative erosion in the Longmen Shan than in the interior of the Sichuan Basin  
436 and Tibetan Plateau (Richardson et al., 2008). This erosive term has the same derivation as  
437 the classic Culling model (Culling, 1960), but assumes that eroded material is removed from  
438 the model domain. This assumption is consistent with Hubbard et al.'s (2010) proposal that  
439 sediment is transported away from the Sichuan basin by the Yangtze River.

440

### 3.3 Lateral Boundary Conditions

The mathematical details of the boundary conditions used in our model are given in Appendix A. Here we summarise these boundary conditions and explain their physical motivation.

Initially ( $t = 0$ ), the domain is filled with a 40 km-thick layer of fluid ( $H_0$ , Figure 4), chosen to represent generic, undeformed continental crust. There may have been pre-existing topography in south-east Tibet before the onset of Cenozoic deformation (Burchfiel et al., 1995; Hubbard et al., 2010). However, the shape of this topography is poorly constrained, so we assume an initially uniform layer for simplicity.

At one edge of the model domain ( $y = 0$ ) fluid flows into the region, analogous to the lateral growth of a mountain range, in this case from central Tibet into south-east Tibet. The height of the influx ( $y = 0$ ) boundary is kept constant over time. The normal stress on this boundary is set by the buoyancy force associated with a reservoir of high material (i.e. the central Tibetan Plateau), which can supply fluid to the current at the same rate at which fluid moves away from the boundary (Figure 4; Reynolds et al., 2015). The reference elevation along this boundary,  $S_0$ , is 4.5 km above the surface of the 40 km thick layer in the remainder of the model domain, similar to the mean elevation of the Tibetan Plateau above the Sichuan Basin (Figure 1). The starting topography within the model domain adjacent to this influx boundary has a constant slope in the  $y$  direction (Figure 4); its gradient does not affect the model results after the first few timesteps. Using a fixed-height boundary condition is analogous to assuming that the central Tibetan plateau acts as a reservoir of lithosphere, and has been at its present elevation throughout the development of high topography in south-east Tibet. This simple assumption allows us to isolate the effects of lateral variations in lower-crustal strength in south-east Tibet, and is consistent with palaeoaltimetric

467 data, which suggest that the central plateau has been high since at least the Eocene (e.g.  
468 Rowley and Currie, 2006). We set the velocity parallel to this boundary to zero ( $u = 0$  on  
469  $y = 0$ ), motivated by the small velocity component parallel to the NW boundary of Figure 3.

470

471 At the right-hand end of the domain as shown in Figure 4 ( $y = y_{max}$ ), and beyond the  
472 basins ( $y > y_b$ ), the normal stress on the boundaries is set by the buoyancy force associated  
473 with 40 km-thick crust outside the model domain (e.g. Artyushkov, 1973; Molnar and Tap-  
474 ponnier, 1978; Dalmayrac and Molnar, 1981; Turcotte and Schubert, 2014). This condition  
475 is equivalent to the model domain being surrounded by 40 km-thick crust and experiencing  
476 the associated buoyancy force at the domain boundaries. Using the buoyancy force to set  
477 the normal stress perpendicular to the boundary, rather than anti-parallel to the maximum  
478 topographic gradient, implicitly assumes that the maximum topographic gradient is perpen-  
479 dicular to the boundary. We find that this assumption has little effect on the modelling  
480 results, and makes the calculations much less computationally expensive because we do not  
481 need to iterate over the velocity calculation at each timestep. However, making this assump-  
482 tion does mean that we require a second condition for the boundary-parallel velocity. We set  
483 the derivatives of boundary-parallel velocities perpendicular to these boundaries to zero (i.e.  
484  $\frac{\partial u}{\partial y} = 0$  on  $y = y_{max}$ , and  $\frac{\partial v}{\partial x} = 0$  on  $x = 0$  and  $x = x_{max}$ ). This second condition is equiv-  
485 alent to assuming that the crust outside the model domain does not exert significant shear  
486 stresses on the domain boundary. These boundary conditions are consistent with the lack  
487 of significant zones of strike-slip deformation outside the region of south-east Tibet which  
488 corresponds to our model domain (Figure 3).

489

490 Along  $x = 0$  and  $x = x_{max}$  we use a reflection boundary condition up to the end of the  
491 basins ( $y < y_b$ ). This is equivalent to assuming that mountains also exist to either side of  
492 the model domain, and are behaving in the same manner in these regions; analogous to high

493 topography existing to the north of the Sichuan Basin and the Central Lowlands of Myanmar.

494

## 495 **4 Results & Comparison to South East Tibet**

496 We initially use symmetric models (i.e. where the two basins with strong lower crust have  
497 the same size and are the same distance from the influx boundary) to investigate the effects  
498 of changing basal thickness and inter-basin width (defined in Figure 4) on the evolution of  
499 topography. Figure 5 shows the results of a model with symmetric basins of radius 450 km  
500 (grey semi-circles, Figure 5c, equivalent to an inter-basin width of 600 km), and basal thick-  
501 ness 15 km. Times referred to are since the start of the model and elevations are given  
502 relative to the surface of 40 km-thick, isostatically-compensated crust. As discussed in Sec-  
503 tion 3, the velocity and, therefore, the rate of topographic evolution, scale linearly with the  
504 viscosity. The topography after 50 Myr of model evolution with a viscosity of  $10^{22}$  Pas (as  
505 shown in Figure 5a) would correspond to that after 5 Myr for a viscosity of  $10^{21}$  Pas.

506

507 Regions with a stress-free base develop gentle topographic gradients. Deformation in  
508 these regions is effectively by pure shear of vertical planes; gentle topographic gradients re-  
509 sult from the quasi-depth-independent horizontal velocities. Gentle topographic gradients  
510 are also a feature of thin-viscous-sheet models (England and McKenzie, 1982, 1983, even  
511 where these models use high stress-exponents; Section 3.1), which have the same, stress-free,  
512 basal boundary condition. The topographic gradients in the stress-free regions are very sim-  
513 ilar in magnitude to the south-eastwards topographic gradients in the high region between  
514 the Sichuan Basin and the Central Lowlands of Myanmar (compare Figures 6h and 6f – the  
515 topographic profile location is shown in Figure 2a).

516

517 In contrast, steep topographic gradients develop in the basin regions, suggesting that  
518 steep topography can form as a result of mountain ranges overriding rigid lower crust. The  
519 different topographic gradients which develop in regions with and without a rigid base (com-  
520 pare Figures 6a, c and e to Figures 6b, d and f), are consistent with previous work showing  
521 that flow over a rigid base results in steeper gradients than flow over a stress-free base (e.g.  
522 McKenzie et al., 2000). The topography also propagates more slowly in the basin regions  
523 than in the region between them (compare Figure 6 c and d). These effects arise because  
524 where flow occurs over a rigid base, the velocity depends on the square of the flow depth  
525 (Huppert, 1982). Increasing the basal thickness, analogous to having a thicker rigid lower  
526 crust or a thinner overlying layer of deformable rock, therefore, reduces the distance which  
527 the current propagates into the basin in a given time, and also results in steeper topographic  
528 profiles where the flow overrides the basin. This effect is demonstrated by Figure 6, which  
529 shows profiles through models with the same basin locations as in Figure 5, but with varying  
530 basal thicknesses. The locations of these profiles are shown in Figure 5b. The lateral extent  
531 of the region which has a rigid base is shown by grey bars on the profiles. Figures 6 a & b,  
532 c & d and e & f have basal thicknesses of 0 km (only the base is rigid), 15 km and 30 km  
533 respectively. A proportionally thicker rigid region (e.g. Figure 6e) means that the current is  
534 flowing into a thinner fluid layer, so tends to develop a sharper nose, as shown by McKenzie  
535 et al. (2000). The topographic gradients across the Longmen Shan (Figures 6g) are very  
536 similar to those in our model for a basal thickness of 30 km (corresponding to 10 km initial  
537 thickness of deformable rock in the basin regions). This basal thickness is consistent with  
538 ~10 km of sediment overlying Paleoproterozoic basement in the Sichuan Basin (Hubbard  
539 and Shaw, 2009).

540

541 Erosion also leads to steeper topographic gradients, and hinders current propagation in  
542 the basins. The dashed lines in Figure 6c and d show the results of eroding the topography

543 with  $\kappa = 4 \text{ mm yr}^{-1}$  in equation (1). The erosive term we use is proportional to gradient  
544 (Section 3), meaning that the steep slopes in the basins are affected more than gentle slopes  
545 in the inter-basin region (compare dashed lines in Figures 6c and d). With  $\kappa = 4 \text{ mm yr}^{-1}$  the  
546 topography is quasi-stationary on the basin margins between 15 and 50 Myr (dashed blue  
547 and red lines in Figure 6c), demonstrating that erosion can stop the propagation of topog-  
548 raphy in these regions (as suggested by Koons, 1989, for the South Island of New Zealand),  
549 but not in the region of fast flow between the basins. The similar position of the present-day  
550 Longmen Shan and the Paleogene deformation front adjacent to the Sichuan Basin (derived  
551 from stratigraphic thicknesses of foreland basin sediments; Richardson et al., 2008) could,  
552 therefore, result from erosion acting on topography which would otherwise be propagating  
553 over the basin. Such an effect is possible because of the slow propagation of topography over  
554 rigid lower crust.

555

556 The distance between basins also controls the velocity of the current. Figure 7 shows the  
557 topographic and velocity profiles resulting from different inter-basin widths, with constant  
558 basal thickness (15 km). Greater inter-basin widths result in faster velocities perpendicular  
559 to the profile ( $v$ , Figures 7b, d, f). Flow in the inter-basin region is dominated by simple shear  
560 of horizontal planes – similar to that between two rigid walls (Copley and McKenzie, 2007),  
561 with maximum velocity proportional to width squared. The width of the rapidly deform-  
562 ing region between the Sichuan Basin and the Central Lowlands of Myanmar is  $\sim 500 \text{ km}$ .  
563 Observed GPS velocities relative to Eurasia in the centre of this region are  $\sim 20 \text{ mm yr}^{-1}$ .  
564 Inter-basin velocities in our model are similar to these GPS velocities for an inter-basin width  
565 of 600 km, which suggests that the viscosity we use for our modelling ( $10^{22} \text{ Pas}$ ) is reasonable.

566

567 As discussed in section 3.2, these models do not include flexural support of the topog-  
568 raphy. If we did include flexural support we would not expect to see qualitatively different

569 topography, because the wavelengths associated with such support are small in compari-  
570 son to the scale of our model. Viscous models of the crust, such as the one we use here,  
571 implicitly investigate long wavelength deformation, at scales longer than individual faults  
572 (Figure 3, England and McKenzie, 1982, 1983). Gravity anomalies demonstrate flexural ef-  
573 fects in south-east Tibet acting on wavelengths less than  $\sim 50$  km (Fielding and McKenzie,  
574 2012), and isostatic compensation throughout the region of high topography (Jordan and  
575 Watts, 2005; Fielding and McKenzie, 2012). Fielding and McKenzie (2012) found a lower  
576 bound on the elastic thickness of the Sichuan Basin of 10 km (although this value is poorly  
577 constrained since the basin is too small for the full flexural wavelength to be measured) and  
578 an elastic thickness of 7 km for the adjacent high topography. Flexure may provide local  
579 support to the topography where it overthrusts the Sichuan Basin (in our model, over the  
580 horizontally rigid basin). The topographic gradient in this region of our model, therefore,  
581 represents an end-member in which the rigid (zero horizontal velocity) base is free to move  
582 vertically. The other end-member, in which the base cannot move vertically in response to  
583 being loaded, also leads to steep fronts (Huppert, 1982), even when flow is into a layer which  
584 is much thicker than the topography (McKenzie et al., 2000). The rigid nature of the basal  
585 boundary (i.e. the no-slip condition on the base of the fluid) controls the shape of the topog-  
586 raphy, rather than whether or not this boundary is able to deform vertically (McKenzie et al.,  
587 2000). Ball et al. (2019) demonstrated that flexural effects are primarily important near the  
588 nose of a viscous current, but that such currents over a flexed base can still form steep  
589 topographic gradients as long as the base of the current has a no-slip boundary condition.  
590 The difference in basal boundary conditions, and the depth of deformable rock, therefore,  
591 provide a first-order explanation for contrasting topographic gradients in south-east Tibet,  
592 even if our models do not capture the precise, short-wavelength details of the topography.

593

594 The elevation histories of particles we track at the surface of the current (Figure 5d)

595 show that uplift rates from our model are  $\sim 0.1\text{--}0.5\text{ mm yr}^{-1}$  in the centre of the inter-  
596 basin region (red star in Figure 5d), similar to the  $< 0.3\text{ mm yr}^{-1}$  uplift rates derived from  
597 palaeoaltimetry (Section 2, Figure 2). However, our modelling also demonstrates that the  
598 interpretation of palaeoelevation results is not straightforward. Figure 5 shows that ma-  
599 terial at the surface may be transported long distances (hundreds of kilometres over tens  
600 of millions of years for the viscosity used here). The advection of particles with the flow  
601 means that elevation histories may be complex, with particle elevations decreasing “south”  
602 (towards  $y = y_{max}$ ) of the inter-basin region as the current spreads laterally (the same effect  
603 which leads to the extensional strain rates described below). Pedogenic carbonates which  
604 are found to have been high in the late Eocene–early Miocene (Hoke et al., 2014; Li et al.,  
605 2015; Gourbet et al., 2017) could have been deposited at similar latitudes to samples from  
606 the Longmen Shan, which were at their present elevation in the late Miocene (Xu et al., 2016).  
607

608 By considering the principal axes of the horizontal the strain-rate tensor at the surface  
609 of our model (Figure 5b) as analogous to the strain rate in the brittle crust (Houseman  
610 and England, 1986), we can draw comparisons between our model and the geodetic- and  
611 seismic-strain rates in south-east Tibet. The largest strain-rates in both our model and in  
612 south-east Tibet are associated with shear at the basin margins. Strain rates equivalent to  
613 left-lateral shear adjacent to Basin E (Figure 4), and right-lateral shear adjacent to Basin  
614 W (Figure 4) are analogous to left-lateral slip on the Xianshuihe Fault and right-lateral slip  
615 on the Nuijiang and Sagaing Faults (and adjacent right-lateral faults) respectively.

616

617 Compressive strain rates associated with steep topography at the edges of the basins are  
618 small in comparison to these shear strain rates. In the context of south-east Tibet this sug-  
619 gests that the steep topography, and low shortening rates, across the Longmen Shan could  
620 result from flow of weaker material, with a coherently-deforming upper and lower crust, over

621 the rigid lower crust of the Sichuan Basin (Copley and McKenzie, 2007; Copley, 2008; Field-  
622 ing and McKenzie, 2012), without a low-viscosity, lower-crustal channel.

623

624 The principal axes of the horizontal strain-rate tensor at the surface of our models show  
625 two extension-dominated regions (red ellipses in Figure 5b), with similar locations and ori-  
626 entations to the normal faulting in south-east Tibet (red ellipses and focal mechanisms in  
627 Figure 1b). The extensional strain rates in these parts of our model are  $\sim 2$ – $5$  times larger  
628 than the compressional strain rates, so these regions are equivalent to mixed strike-slip and  
629 normal faulting, with normal faulting dominating. Extension in the y direction ‘north’ of  
630 the basins (top white ellipse in Figure 5b) is comparable to the northern group of normal  
631 faults in Figure 1, which strike perpendicular to both topographic gradient (accommodat-  
632 ing extension parallel to the topographic gradient) and GPS velocities relative to Eurasia  
633 (Figure 3). Our modelling suggests that this extension may result from a velocity increase  
634 where the topography is confined in the inter-basin region. The second region of extension  
635 occurs where fluid spreads out laterally to the ‘south’ of the basins; increasing the surface  
636 area of the current. This extension perpendicular to topographic gradients is shown by the  
637 bottom white ellipse in Figure 5b. The southern group of normal faults shown in Figure 1  
638 also accommodate extension perpendicular to the topographic gradients.

639

640 Figure 8 shows the results of changing the shape of one of the basins to be more similar  
641 to that of the Central Lowlands of Myanmar. The region of shear which develops adja-  
642 cent to this basin is broader than that adjacent to a semi-circular basin because the flow  
643 is approximately parallel to the change in basal boundary condition, resulting in greater  
644 horizontal tractions on vertical planes. This broader region of shear is similar to the area of  
645 distributed left-lateral faulting east of the Sagaing fault (Figure 1a), which accommodates  
646 right-lateral shear through vertical-axis rotations (Copley, 2008). The lateral extent of this

647 shear in south-east Tibet may, therefore, be controlled by the geometry of the rigid lower  
648 crust in the Central Lowlands of Myanmar.

649

## 650 **5 Discussion**

651 Our model allows us to reproduce the main features of the present-day topography, strain-  
652 rate and velocity field in south-east Tibet, and uplift rates from palaeoaltimetry. These  
653 results demonstrate that lateral strength contrasts, in the form of regions of rigid lower  
654 crust, provide a first-order control on the temporal evolution of mountain ranges (Figure 9).  
655 Below we discuss our key findings and their application to mountain ranges in general.

656

657 In our model, which has mechanically-coupled upper and lower crust, surface uplift rates  
658 are  $<0.5 \text{ mm yr}^{-1}$ . These gradual uplift rates are consistent with palaeoaltimetry results in  
659 south-east Tibet, suggesting that no low-viscosity, lower-crustal channel is required to ex-  
660 plain to evolution of topography in this region. However, the results of particle tracking show  
661 that material at the surface where the crust flows over a stress-free base may be transported  
662 long distances (hundreds of kilometres over millions of years for the viscosity used here,  
663 consistent with fault offsets reported over shorter time periods, Wang and Burchfiel, 1997).  
664 Calculated palaeoelevations, therefore, estimate the palaeoelevation of the place where the  
665 sample was deposited, rather than the palaeoelevation of its present-day location. Account-  
666 ing for this lateral transport is also important for converting the oxygen-isotope composition  
667 of carbonates to palaeoelevation, potentially requiring greater continentality corrections. Al-  
668 though strike-slip faults do not build mountains, they can move them horizontally for large  
669 distances.

670

671 Our modelling demonstrates that differences in basal boundary condition, analogous to  
672 the presence or absence of strong lower crust, can lead to the development of contrasting  
673 topographic gradients. In particular, steep gradients arise naturally from flow over a rigid  
674 (no-slip) base. The present-day compressional strain rates across these steep margins are  
675 low in comparison to the rates of shear where deformation is parallel to the basin margins,  
676 in both our model and in south-east Tibet (Shen et al., 2005; Zheng et al., 2017). This  
677 combination, of steep-fronted topography and low compressional strain rates, is a feature of  
678 other parts of the India-Eurasia collision. Steep topographic gradients adjacent to the Tarim  
679 basin ( $\sim 3$  km over 50 km) and the low rate of shortening ( $0\text{--}3$  mm yr $^{-1}$ , e.g. Zheng et al.,  
680 2017) across the basin margin are similar to those in the Longmen Shan. Increasing Moho  
681 depths from north to south across the margin (Wittlinger et al., 2004), and the flexural sig-  
682 nal seen in free-air gravity anomalies (e.g. McKenzie et al., 2019), suggests that the western  
683 edge of the Tarim Basin may underthrust the western Kunlun ranges, which would provide  
684 a rigid base to the flow of crustal material from northern Tibet, in a similar manner to the  
685 Sichuan Basin in south-east Tibet. The temporal evolution of topography adjacent to the  
686 Tarim Basin may, therefore, also be controlled by the lateral strength contrast between rigid  
687 lower crust in the Tarim Basin and lower viscosity crust in Tibet. The motion of southern  
688 Tibet over rigid India is likely to represent the same effect. However, the rates of motion  
689 in southern Tibet are more rapid than in northern Tibet, perhaps due to differences in the  
690 thicknesses, temperatures or compositions of the crust in India and the Tarim basin.

691

692 More generally, the control on topographic evolution provided by lateral strength con-  
693 trasts, particularly the low rates of propagation of topography into regions with rigid lower  
694 crust (Figures 6, 9), suggests an explanation for the correlation of cratonic regions with steep  
695 edges of mountain belts (including the Atlas mountains, the Caucasus and older orogenies  
696 such as the Appalachians and Rockies in North America) noted by McKenzie and Priestley

697 (2008). Cratonic regions are likely to have relatively strong lower crust (e.g. Jackson et al.,  
698 2008), so our results suggest that the propagation of topography into these regions will be  
699 slow in comparison to adjacent regions where the lower crust has lower viscosity.

700

701 We also find that the thickness of strong lower crust, and of deformable material (such as  
702 sediments) above it, controls the extent of mountain range propagation and the morphology  
703 of the range front. Larger thicknesses of deformable rock (fluid layer above the rigid base  
704 in our models) lead to more rapid propagation of topography over regions with strong lower  
705 crust, and to shallower topographic gradients. This result is likely to apply to mountain  
706 ranges globally. The occurrence of thin-skinned deformation of sediments above the edges of  
707 the South American craton, in the foothills of the Eastern Cordillera of the Andes (Lamb,  
708 2000), suggests that the deformation in this region is comparable to flow over a rigid base.  
709 The foothills in the southern Bolivian Andes extend further east than those in the north,  
710 and have lower topographic gradients. This broader foothill region correlates with higher  
711 sediment thicknesses in the bounding basin (McGroder et al., 2014), similar to the current  
712 in our model propagating further over a rigid base where the deformable layer is thicker  
713 (Figure 6c and e). Along-strike variations in sediment thickness can also explain variations  
714 in the morphology of the Indo-Burman Ranges (Ball et al., 2019), although there moun-  
715 tain building is driven by the subducting plate, which advects sediment laterally, as well as  
716 by contrasts in gravitational potential energy. Ball et al. (2019) highlighted that it is the  
717 thickness of deformable sediment, rather than the total sediment thickness, which is impor-  
718 tant in controlling morphology. Although beyond the scope of this study, we expect that  
719 along-strike variations in the viscosity of the deformable rock, as well as its thickness, could  
720 lead to similar changes in morphology. In the Zagros mountains, for example, along-strike  
721 variations in the width of high topography could potentially correlate with the presence or  
722 absence of weak salt layers (Nissen et al., 2011). Similarly, the prominent curvature of the

723 Sulaiman Ranges, and their projection beyond the general  $\sim$ north–south strike of the Pak-  
724 istan range front, has been proposed to result from a weaker package of sediments beneath  
725 them (Reynolds et al., 2015).

726

727 For crust in this tectonic setting, it is not clear whether ductile deformation is dominated  
728 by diffusion creep, which is Newtonian with a stress exponent of 1, or dislocation creep,  
729 which has a power-law rheology with a stress exponent greater than 1, (e.g. Stocker and  
730 Ashby, 1973). In our modelling, we have, therefore, taken the simplest approach, which  
731 is to use a Newtonian rheology with a constant viscosity. Our models show that such a  
732 rheology can produce steep topographic gradients where flow occurs over a rigid base, such  
733 as strong lower crust. In contrast, in models where depth variations in horizontal velocity  
734 are neglected, steep topographic gradients require a power-law rheology with a high stress  
735 exponent, and, even then, these gradients are much shallower than those in the Longmen  
736 Shan (Section 3.1, Houseman and England, 1986; England and Houseman, 1986; Lechmann  
737 et al., 2011). If dislocation creep does control ductile deformation, the vertically-integrated  
738 strength of the lithosphere can be represented as a single power-law rheology (Sonder and  
739 England, 1986). An interesting question, therefore, is whether the steep topographic gradi-  
740 ents in our model would still form if we had used a power-law, rather than a Newtonian,  
741 rheology. A higher stress-exponent would tend to localise deformation in regions of high  
742 strain rate, such as immediately above the rigid lower crust in the basin regions. The second  
743 invariant of the strain rate tensor in these regions of our model is  $\sim 10^{-15} \text{ s}^{-1}$ , consistent with  
744 geodetically- and geologically-estimated strain rates in tectonically active regions (Fagereng  
745 and Biggs, 2019). For a viscosity of  $10^{22} \text{ Pas}$  this strain rate corresponds to a stress of  
746  $\sim 10 \text{ MPa}$ , typical of earthquake stress drops (Kanamori and Anderson, 1975; Allmann and  
747 Shearer, 2009). If the crust were to deform with a power-law rheology with a stress-exponent  
748 of 3, and assuming a strain rate in the rest of the model domain of  $\sim 10^{-16} \text{ s}^{-1}$ , these strain

749 rates would lead to a local drop in viscosity from  $10^{22}$  Pas to  $\sim 2 \times 10^{21}$  Pas, which might  
750 lubricate the base of the current. However, the flow over the rigid base would still be much  
751 slower than that with a stress-free base, and have a non-linear dependence on the thickness  
752 of the current, meaning that we would still expect contrasting topographic gradients to de-  
753 velop. Mathematical studies of gravity currents composed of power-law fluids suggest that,  
754 although there may be some increase in far-field surface slope associated with such effects,  
755 flow over a rigid base nonetheless tends to produce a steep front (Gratton et al., 1999).  
756 Our result, that steep topographic gradients can form with a Newtonian rheology, therefore,  
757 suggests that steep-fronted mountain ranges do not constrain whether flow in the ductile  
758 part of the lithosphere occurs by diffusion or dislocation creep, but does demonstrate that  
759 the presence of strong lower crust can explain first-order contrasts in topographic gradients.

760

## 761 **6 Conclusion**

762 We have investigated the role of lateral contrasts in lower crustal strength in controlling the  
763 shape and evolution of mountain ranges. In south-east Tibet, stable-isotope palaeoaltimetry  
764 suggests that parts of the topography may have been at, or near, their present-day elevations  
765 since the late Eocene and that uplift is likely to have occurred more slowly than had pre-  
766 viously been inferred. In combination with a simple model, these results demonstrate that  
767 lateral strength contrasts are sufficient to explain first-order features of the deformation and  
768 topographic evolution in south-east Tibet, without invoking a low-viscosity, lower-crustal  
769 channel. Since our models of topographic evolution in the presence of lateral lower-crustal  
770 strength contrasts allow us to reproduce the main features of the present day topography,  
771 strain-rate and velocity field in south-east Tibet, we suggest that lateral strength contrasts  
772 provide a first-order control on the temporal evolution and shape of mountain ranges. Our

773 modelling also suggests that lateral contrasts in lower crustal strength provide an explanation  
774 for the correlation between cratons and the steep gradients on the edges of some mountain  
775 ranges.

## 776 **Acknowledgements**

777 C.P. would like to thank Thomasina Ball and Jerome Neufeld for helpful discussions. This  
778 work forms part of the NERC- and ESRC-funded project ‘Earthquakes without Frontiers’  
779 and was partially supported by the NERC large grant ‘Looking inside the Continents from  
780 Space’. C.P. is funded by a Junior Research Fellowship from Queens’ College, University of  
781 Cambridge and was funded by a NERC studentship for part of the research. Figures were  
782 prepared using the GMT package (Wessel et al., 2013). No data was created for this research.  
783 Palaeoaltimetry data can be found in Hoke et al. (2014); Li et al. (2015); Xu et al. (2016);  
784 Tang et al. (2017); Gourbet et al. (2017); Wu et al. (2018). Earthquake focal mechanisms  
785 can be found in Copley (2008) (and references therein), Zhang et al. (2010), Li et al. (2011),  
786 Han et al. (2014), Bai et al. (2017), Han et al. (2018), the CMT catalogue (Dziewonski et al.,  
787 1981; Ekström et al., 2012) and the ISC-EHB catalogue (Engdahl et al., 1998; International  
788 Seismological Centre, 2016). GPS data in Figure 3 are from Zheng et al. (2017).

## A Time evolution of a viscous current

We solve the Stokes' flow equations, neglecting horizontal variations in vertical velocity, following the method proposed by Pattyn (2003) for glaciers. We briefly outline this method below in order to demonstrate how our model results are calculated and to highlight some possible simplifications.

In a Cartesian co-ordinate system,  $(x, y, z)$ , the horizontal velocities  $(u, v)$  are related to gradients of the surface height,  $s$ , through:

$$4\frac{\partial\eta}{\partial x}\frac{\partial u}{\partial x} + \frac{\partial\eta}{\partial y}\frac{\partial u}{\partial y} + \frac{\partial\eta}{\partial z}\frac{\partial u}{\partial z} + \eta\left(4\frac{\partial^2}{\partial x^2} + \frac{\partial^2}{\partial y^2} + \frac{\partial^2}{\partial z^2}\right)u = \rho g\frac{\partial s}{\partial x} - 2\frac{\partial\eta}{\partial x}\frac{\partial v}{\partial y} - \frac{\partial\eta}{\partial y}\frac{\partial v}{\partial x} - 3\eta\frac{\partial^2 v}{\partial x\partial y} \quad (1)$$

and

$$4\frac{\partial\eta}{\partial y}\frac{\partial v}{\partial y} + \frac{\partial\eta}{\partial x}\frac{\partial v}{\partial x} + \frac{\partial\eta}{\partial z}\frac{\partial v}{\partial z} + \eta\left(\frac{\partial^2}{\partial x^2} + 4\frac{\partial^2}{\partial y^2} + \frac{\partial^2}{\partial z^2}\right)v = \rho g\frac{\partial s}{\partial y} - \frac{\partial\eta}{\partial x}\frac{\partial u}{\partial y} - 2\frac{\partial\eta}{\partial y}\frac{\partial u}{\partial x} - 3\eta\frac{\partial^2 u}{\partial x\partial y} \quad (2)$$

(equations 18 and 19 of Pattyn, 2003) where  $\eta$  and  $\rho$  are the viscosity and density of the fluid respectively, and  $g$  is the gravitational acceleration. We follow Pattyn in scaling the vertical dimension at each timestep (cf. his equation 44). We then solve the resulting velocity equations at each timestep (subject to the boundary conditions discussed below and in section 3.3) using the generalised minimum residual method (Saad and Schultz, 1986, in sparskit2).

We include the full form of these equations here to illustrate the general, variable viscosity case. However, since we consider the constant viscosity case here,  $\nabla\eta = \mathbf{0}$  and these equations

can be simplified to

$$\eta \left( 4 \frac{\partial^2}{\partial x^2} + \frac{\partial^2}{\partial y^2} + \frac{\partial^2}{\partial z^2} \right) u = \rho g \frac{\partial s}{\partial x} - 3\eta \frac{\partial^2 v}{\partial x \partial y} \quad (3)$$

and

$$\eta \left( \frac{\partial^2}{\partial x^2} + 4 \frac{\partial^2}{\partial y^2} + \frac{\partial^2}{\partial z^2} \right) v = \rho g \frac{\partial s}{\partial y} - 3\eta \frac{\partial^2 u}{\partial x \partial y}. \quad (4)$$

Taking partial derivatives of the incompressibility condition,

$$\frac{\partial u}{\partial x} + \frac{\partial v}{\partial y} + \frac{\partial w}{\partial z} = 0, \quad (5)$$

with respect to  $x$  and  $y$ , and using the conditions  $\frac{\partial w}{\partial x}, \frac{\partial w}{\partial y} = 0$  (section 3.2) gives

$$\frac{\partial^2 u}{\partial x^2} + \frac{\partial^2 v}{\partial x \partial y} = 0, \quad (6)$$

and

$$\frac{\partial^2 v}{\partial y^2} + \frac{\partial^2 u}{\partial y \partial x} = 0. \quad (7)$$

Equations (3) and (4) then reduce to

$$\left( \frac{\partial^2}{\partial x^2} + \frac{\partial^2}{\partial y^2} + \frac{\partial^2}{\partial z^2} \right) u = \frac{\rho g}{\eta} \frac{\partial s}{\partial x} \quad (8)$$

and

$$\left( \frac{\partial^2}{\partial x^2} + \frac{\partial^2}{\partial y^2} + \frac{\partial^2}{\partial z^2} \right) v = \frac{\rho g}{\eta} \frac{\partial s}{\partial y}. \quad (9)$$

805

806

807 Pattyn (2003) proposed rewriting the incompressibility condition as a diffusion equation  
 808 for topography. This approach allows the diffusivities to be calculated on a staggered grid,  
 809 preventing leapfrog instabilities in the second-order finite differences. From integrating the  
 810 incompressibility condition (5) over the layer thickness,  $H$  (Figure 4):

$$\frac{\partial H}{\partial t} = -\nabla_h \cdot (H\bar{u}, H\bar{v}), \quad (10)$$

811 where bars denote vertical averaging, and

$$\nabla_h = \left( \frac{\partial}{\partial x}, \frac{\partial}{\partial y} \right). \quad (11)$$

812 Equation (10) can be written as a diffusion equation for the topography, which Pattyn (2003)  
 813 expressed as:

$$\frac{\partial H}{\partial t} = \nabla_h \cdot \left( D_x \frac{\partial H}{\partial x}, D_y \frac{\partial H}{\partial y} \right) + \nabla_h \cdot \left( D_x \frac{\partial b}{\partial x}, D_y \frac{\partial b}{\partial y} \right), \quad (12)$$

(his equation 55, where we make the derivatives explicit here for clarity), and:

$$D_x = \left| \bar{u} H \left( \frac{\partial s}{\partial x} \right)^{-1} \right|,$$

$$D_y = \left| \bar{v} H \left( \frac{\partial s}{\partial y} \right)^{-1} \right|,$$

(the modulus signs were implied but not included in Pattyn, 2003). In the glacier case for which this method was developed there is no prescribed relationship between the surface height,  $s$ , and bed depth,  $b$  (although  $H = s + b$ ). However, for an isostatically-compensated fluid, such as the crust of south-east Tibet (e.g. Jordan and Watts, 2005),  $b = -fs$  and  $H = (1 + f)s$ , where  $f = \frac{\rho_c}{\rho_m - \rho_c}$ . For standard crust and mantle densities of 2700 kg m<sup>-3</sup> and

3300 kg m<sup>-3</sup> respectively,  $f = 4.5$ , which is what we assume here. Substituting these relationships into (12) gives

$$\frac{\partial H}{\partial t} = \left( \frac{1}{f+1} \right) (\partial_x (D_x \partial_x H) + \partial_y (D_y \partial_y H)). \quad (13)$$

We note that the diffusivities could alternatively have been defined as

$$D'_x = \left| \bar{u} H \left( \frac{\partial H}{\partial x} \right)^{-1} \right|,$$

$$D'_y = \left| \bar{v} H \left( \frac{\partial H}{\partial y} \right)^{-1} \right|,$$

in which case

$$\frac{\partial H}{\partial t} = (\partial_x (D'_x \partial_x H) + \partial_y (D'_y \partial_y H)). \quad (14)$$

814  $D_n = 0, n \in \{x, y\}$  becomes infinite if  $\frac{\partial s}{\partial n} = 0$ , but physically the topography in such  
 815 regions should not propagate (i.e.  $\frac{\partial H}{\partial t} = 0$ , since in regions of flat topography there are no  
 816 pressure contrasts to drive the flow). In such cases, therefore, we set  $D_n = 0$ .

817

818 We write equation (13) as a sparse matrix equation using a Crank-Nicolson scheme for the  
 819 finite differences, with diffusivities calculated on a staggered grid, the approach suggested by  
 820 Pattyn (2003). Solving both x and y terms in the same linear system, rather than separating  
 821 the components means that the matrix does not have a simple form (the separated case  
 822 is tridiagonal, which was the form used by Reynolds et al., 2015). We therefore solve this  
 823 sparse system using the generalised minimum residual method (Saad and Schultz, 1986).

824 **Boundary Conditions**

825 **Pressure Boundary conditions**

Noting that the NW and SE margins of the region we study are isostatically compensated (e.g. Jordan and Watts, 2005), we impose the deviatoric stress resulting from integrated pressure differences between fluid in the domain and an assumed reservoir outside the domain on  $y \in \{0, y_{max}\}$  and  $x \in \{0, x_{max}\}$  for  $y > y_b$  (where  $y_b$  denotes the far end of the basin, Figure 4). The buoyancy force exerted by a column of thickness  $H_0$  on a column with thickness  $H = H_0 - \Delta H$  is

$$\begin{aligned} \int_{-b}^s \Delta p dz &= -\frac{g\rho_c}{2} \left(1 - \frac{\rho_c}{\rho_m}\right) (H_0^2 - (H_0 - \Delta H)^2) \\ &= -\frac{g\rho_c}{2(1+f)} \Delta H (2H_0 - \Delta H), \end{aligned} \quad (15)$$

826 (e.g. Artyushkov, 1973; Molnar and Tapponnier, 1978; Dalmayrac and Molnar, 1981; Tur-  
827 cotte and Schubert, 2014, Figure A.1), where  $p$  is the lithostatic pressure, giving an associated  
828 deviatoric stress

$$\Delta\sigma_{yy} = -\frac{g\rho_c}{2H(1+f)} \Delta H (2H_0 - \Delta H) = 2\eta \frac{\partial v}{\partial y}, \quad (16)$$

829 on boundaries in  $y$ , and

$$\Delta\sigma_{xx} = -\frac{g\rho_c}{2H(1+f)} \Delta H (2H_0 - \Delta H) = 2\eta \frac{\partial u}{\partial x}, \quad (17)$$

830 on boundaries in  $x$ . We define tensional stresses as positive. Note that  $\Delta H$  could be negative  
831 if the reference thickness is less than the thickness of the adjacent material, as is initially  
832 the case on the outflux boundaries. For the outflux boundaries,  $H_0 = 40$  km. For the  
833 influx ( $y = 0$ ) boundary  $H_0 = 65$  km (corresponding to 4.5 km surface relief above 40 km  
834 thick crust). Ideally, we would impose the stress condition on the outflux boundary anti-

835 parallel to the direction of flow, to represent a uniform reservoir of unthickened crust i.e. the  
836 direction normal to the outflux domain boundaries has no particular physical or geological  
837 significance. We impose the pressure condition on the normal stress for simplicity. As a  
838 result, these boundary conditions determine only the boundary-perpendicular velocities, and  
839 we require a further condition on the boundary-parallel velocities. For the influx boundary,  
840 we set  $u = 0$ . For the outflux boundaries we set  $\frac{\partial v}{\partial x} = 0$  on  $x \in \{0, x_{max}\}$  and  $\frac{\partial u}{\partial y} = 0$  on  
841  $y = y_{max}$ . Since the far-field part of the domain is not substantially thickened by the end of  
842 our modelling, velocities adjacent to these far-field boundaries are small and we expect that  
843 imposing the stresses anti-parallel to the flow would not substantially alter our results.

#### 844 **Reflection Boundary conditions**

On  $x \in \{0, x_{max}\}$  we use reflection boundary conditions  $u = 0$ ,  $\frac{\partial v}{\partial x} = 0$  for  $y < y_b$ . We impose  
the condition on  $u$  directly. As shown above, for constant viscosity,  $v$  is given by equation  
(9), which can be further simplified by considering

$$u|_{x=0} = 0 \Rightarrow \frac{\partial u}{\partial y} \Big|_{x=0} = 0 \Rightarrow \frac{\partial^2 u}{\partial x \partial y} = 0,$$

which, from (7), implies that  $\frac{\partial^2 v}{\partial y^2} = 0$ . Equation (9) therefore reduces to

$$\left( \frac{\partial^2}{\partial x^2} + \frac{\partial^2}{\partial z^2} \right) v = \frac{\rho g}{\eta} \frac{\partial s}{\partial y}, \quad (18)$$

845 which we solve in its co-ordinate transformed form.

## 846 **References**

847 Allmann, B. P. and Shearer, P. M. (2009). Global variations of stress drop for moderate to  
848 large earthquakes. *J. Geophys. Res. Solid Earth*, 114(1):1–22.

- 849 Artyushkov, E. V. (1973). Stresses in the lithosphere caused by crustal thickness inhomogeneities. *J. Geophys. Res.*, 78(32):7675–7708.
- 850
- 851 Bai, L., Li, G., Khan, N. G., Zhao, J., and Ding, L. (2017). Focal depths and mechanisms of shallow earthquakes in the Himalayan-Tibetan region. *Gondwana Res.*, 41:390–399.
- 852
- 853 Ball, T. V., Penney, C. E., Neufeld, J. A., and Copley, A. C. (2019). Controls on the geometry and evolution of thin-skinned fold-thrust belts, and applications to the Makran accretionary prism and Indo–Burman Ranges. *Geophys. J. Int.*, 218(1):247–267.
- 854
- 855
- 856 Beaumont, C., Jamieson, R. A., Nguyen, M. H., and Lee, B. (2001). Himalayan tectonics explained by extrusion of a low-viscosity crustal channel coupled to focused surface denudation. *Nature*, 414(6865):738–742.
- 857
- 858
- 859 Bischoff, S. and Flesch, L. (2019). Impact of Lithospheric Strength Distribution on India-Eurasia Deformation From 3-D Geodynamic Models. *J. Geophys. Res. Solid Earth*, 124(1):1084–1105.
- 860
- 861
- 862 Burchfiel, B. C., Zhiliang, C., Yupinc, L., and Royden, L. H. (1995). Tectonics of the Longmen Shan and Adjacent Regions, Central China. *Int. Geol. Rev.*, 37(8):661–735.
- 863
- 864 Bystricky, M. and Mackwell, S. (2001). Creep of dry clinopyroxene aggregates with deformation in the dislocation creep. *J. Geophys. Res.*, 106:13443–13454.
- 865
- 866 Chen, L., Gerya, T., Zhang, Z., Zhu, G., Duretz, T., and Jacoby, W. R. (2013a). Numerical modeling of eastern Tibetan-type margin: Influences of surface processes, lithospheric structure and crustal rheology. *Gondwana Res.*, 24(3-4):1091–1107.
- 867
- 868
- 869 Chen, L., Gerya, T. V., Zhang, Z. J., Aitken, A., Li, Z. H., and Liang, X. F. (2013b). Formation mechanism of steep convergent intracontinental margins: Insights from numerical modeling. *Geophys. Res. Lett.*, 40(10):2000–2005.
- 870
- 871

- 872 Clark, M. K., Bush, J. W. M., and Royden, L. H. (2005a). Dynamic topography produced  
873 by lower crustal flow against rheological strength heterogeneities bordering the Tibetan  
874 Plateau. *Geophys. J. Int.*, 162:575–590.
- 875 Clark, M. K., House, M. A., Royden, L. H., Whipple, K. X., Burchfiel, B. C., Zhang, X., and  
876 Tang, W. (2005b). Late Cenozoic uplift of southeastern Tibet. *Geology*, 33(6):525–528.
- 877 Clark, M. K. and Royden, L. H. (2000). Topographic ooze: Building the eastern margin of  
878 Tibet by lower crustal flow. *Geology*, 28(8):703.
- 879 Clark, M. K., Royden, L. H., Whipple, K. X., Burchfiel, B. C., Zhang, X., and Tang, W.  
880 (2006). Use of a regional, relict landscape to measure vertical deformation of the eastern  
881 Tibetan Plateau. *J. Geophys. Res. Earth Surf.*, 111:F03002.
- 882 Clark, M. K., Schoenbohm, L. M., Royden, L. H., Whipple, K. X., Burchfiel, B. C., Zhang,  
883 X., Tang, W., Wang, E., and Chen, L. (2004). Surface uplift, tectonics, and erosion of  
884 eastern Tibet from large-scale drainage patterns. *Tectonics*, 23:TC1006.
- 885 Cook, K. L. and Royden, L. H. (2008). The role of crustal strength variations in shaping  
886 orogenic plateaus, with application to Tibet. *J. Geophys. Res. Solid Earth*, 113(8):1–18.
- 887 Copley, A. (2008). Kinematics and dynamics of the southeastern margin of the Tibetan  
888 Plateau. *Geophys. J. Int.*, 174:1081–1100.
- 889 Copley, A. and McKenzie, D. (2007). Models of crustal flow in the India-Asia collision zone.  
890 *Geophys. J. Int.*, 169:683–698.
- 891 Culling, W. E. H. (1960). Analytical Theory of Erosion. *J. Geol.*, 68(3):336–344.
- 892 Dalmayrac, B. and Molnar, P. (1981). Parallel thrust and normal faulting in Peru and  
893 constraints on the state of stress. *Earth Planet. Sci. Lett.*, 55:473–481.

- 894 Dziewonski, A. M., Chou, T., and Woodhouse, J. H. (1981). Determination of earthquake  
895 source parameters from waveform data for studies of global and regional seismicity. *J.*  
896 *Geophys. Res.*, 86(B4):2825–2852.
- 897 Ekström, G., Nettles, M., and Dziewoński, A. M. (2012). The global CMT project 2004-2010:  
898 Centroid-moment tensors for 13,017 earthquakes. *Phys. Earth Planet. Inter.*, 200-201:1–9.
- 899 Engdahl, E. R., van der Hilst, R., and Buland, R. (1998). Global teleseismic earthquake  
900 relocation with improved travel times and procedures for depth determination. *Bull.*  
901 *Seismol. Soc. Am.*, 88(3):722–743.
- 902 England, P. and Houseman, G. (1985). Role of lithospheric strength heterogeneities in the  
903 tectonics of Tibet and neighbouring regions. *Nature*, 315:297–301.
- 904 England, P. and Houseman, G. (1986). Finite strain calculations of continental deforma-  
905 tion: 2. Comparison with the India-Asia Collision Zone. *J. Geophys. Res. Solid Earth*,  
906 91(B3):3664–3676.
- 907 England, P. and McKenzie, D. (1982). A thin viscous sheet model for continental deforma-  
908 tion. *Geophys. J. Int.*, 70:295–321.
- 909 England, P. and McKenzie, D. (1983). Correction to: a thin viscous sheet model for conti-  
910 nental deformation. *Geophys. J. R. Astr. Soc.*, 73:523–532.
- 911 Fagereng, Å. and Biggs, J. (2019). New perspectives on ‘geological strain rates’ calculated  
912 from both naturally deformed and actively deforming rocks. *J. Struct. Geol.*, 125(January  
913 2018):100–110.
- 914 Fielding, E. J. and McKenzie, D. (2012). Lithospheric flexure in the Sichuan Basin and  
915 Longmen Shan at the eastern edge of Tibet. *Geophys. Res. Lett.*, 39:L09311.

- 916 Flesch, L., Bendick, R., and Bischoff, S. (2018). Limitations on Inferring 3D Architecture  
917 and Dynamics From Surface Velocities in the India-Eurasia Collision Zone. *Geophys. Res.*  
918 *Lett.*, 45:1379–1386.
- 919 Flesch, L. M., Haines, J. A., and Holt, W. E. (2001). Dynamics of the India-Eurasia Short-  
920 ening. *J. Geophys. Res.*, 106(B8):16,435–16,460.
- 921 Gourbet, L., Hervé, P., Paquette, J.-L., Sorrel, P., Maheo, G., Wang, G., Yadong, X.,  
922 Cao, K., Antoine, P.-O., Eymard, I., Liu, W., Lu, H., Replumaz, A., Chevalier, M.-L.,  
923 Kexin, Z., Jing, W., and Shen, T. (2017). Reappraisal of the Jianchuan Cenozoic basin  
924 stratigraphy and its implications on the SE Tibetan plateau evolution. *Tectonophysics*,  
925 700-701:162–179.
- 926 Gratton, J., Minotti, F., and Mahajan, S. M. (1999). Theory of creeping gravity currents of  
927 a non-Newtonian liquid. *Phys. Rev. E - Stat. Physics, Plasmas, Fluids, Relat. Interdiscip.*  
928 *Top.*, 60(6):6960–6967.
- 929 Han, L., Cheng, J., An, Y., Fang, L., Jiang, C., Chen, B., Wu, Z., Liu, J., Xu, X., Liu, R.,  
930 Yao, Z., Wang, C., and Wang, Y. (2018). Preliminary Report on the 8 August 2017 Ms  
931 7.0 Jiuzhaigou, Sichuan, China, Earthquake. *Seismol. Res. Lett.*, 89(2A):557–569.
- 932 Han, L., Zeng, X., Jiang, C., Ni, S., Zhang, H., and Long, F. (2014). Focal Mechanisms of  
933 the 2013 Mw 6.6 Lushan, China Earthquake and High-Resolution Aftershock Relocations.  
934 *Seismol. Res. Lett.*, 85(1):8–14.
- 935 Hoke, G. D. (2018). Geochronology transforms our view of how Tibet’s southeast margin  
936 evolved. *Geology*, 46(1):95–96.
- 937 Hoke, G. D., Liu-Zeng, J., Hren, M. T., Wissink, G. K., and Garzione, C. N. (2014). Stable  
938 isotopes reveal high southeast Tibetan Plateau margin since the Paleogene. *Earth Planet.*  
939 *Sci. Lett.*, 394:270–278.

- 940 Holmes, A. (1965). *The Principles of Physical Geology*. Nelson, Edinburgh.
- 941 Houseman, G. and England, P. (1986). Finite strain calculations of continental deformation.  
942 1. Method and general results for convergence zones. *J. Geophys. Res.*, 91(B3):3651–3663.
- 943 Hren, M. T., Bookhagen, B., Blisniuk, P. M., Booth, A. L., and Chamberlain, C. P. (2009).  
944  $\delta^{18}\text{O}$  and  $\delta\text{D}$  of streamwaters across the Himalaya and Tibetan Plateau: Implications for  
945 moisture sources and paleoelevation reconstructions. *Earth Planet. Sci. Lett.*, 288:20–32.
- 946 Huang, M. H., Bürgmann, R., and Freed, A. M. (2014). Probing the lithospheric rheology  
947 across the eastern margin of the Tibetan Plateau. *Earth Planet. Sci. Lett.*, 396:88–96.
- 948 Hubbard, J. and Shaw, J. H. (2009). Uplift of the Longmen Shan and Tibetan plateau, and  
949 the 2008 Wenchuan ( $M = 7.9$ ) earthquake. *Nature*, 458:194–197.
- 950 Hubbard, J., Shaw, J. H., and Klinger, Y. (2010). Structural setting of the 2008 Mw7.9  
951 Wenchuan, China, earthquake. *Bull. Seismol. Soc. Am.*, 100(5B):2713–2735.
- 952 Huppert, H. E. (1982). The propagation of two-dimensional and axisymmetric viscous gravity  
953 currents over a rigid horizontal surface. *J. Fluid Mech.*, 121:43–58.
- 954 International Seismological Centre (2016). EHB Bulletin.
- 955 Jackson, J., McKenzie, D., Priestley, K., and Emmerson, B. (2008). New views on the  
956 structure and rheology of the lithosphere. *J. Geol. Soc. London.*, 165:453–465.
- 957 Jordan, T. A. and Watts, A. B. (2005). Gravity anomalies, flexure and the elastic thickness  
958 structure of the India-Eurasia collisional system. *Earth Planet. Sci. Lett.*, 236(3-4):732–  
959 750.
- 960 Kanamori, H. and Anderson, D. (1975). Theoretical basis of some empirical relations in  
961 seismology. *B. Seism. Soc. Am.*, 65(5):1073–1095.

- 962 Kirby, E., Reiners, P. W., Krol, M. A., Whipple, K. X., Hodges, K. V., Farley, K. A., Tang,  
963 W., and Chen, Z. (2002). Late Cenozoic evolution of the eastern margin of the Tibetan  
964 Plateau: Inferences from  $^{40}\text{Ar}/^{39}\text{Ar}$  and (U-Th)/He thermochronology. *Tectonics*,  
965 21(1):1001–1019.
- 966 Koons, P. O. (1989). The topographic evolution of collisional mountain belts: a numerical  
967 look at the Southern Alps, New Zealand. *Am. J. Sci.*, 289(9):1041–1069.
- 968 Lamb, S. (2000). Active deformation in the Bolivian Andes, South America. *J. Geophys.*  
969 *Res. Solid Earth*, 105(B11):25627–25653.
- 970 Lebedev, S. and Nolet, G. (2003). Upper mantle beneath Southeast Asia from S velocity  
971 tomography. *J. Geophys. Res. Solid Earth*, 108(B1).
- 972 Lechmann, S. M., May, D. A., Kaus, B. J., and Schmalholz, S. M. (2011). Comparing  
973 thin-sheet models with 3-D multilayer models for continental collision. *Geophys. J. Int.*,  
974 187(1):10–33.
- 975 Lechmann, S. M., Schmalholz, S. M., Hetényi, G., May, D. A., and Kaus, B. J. P. (2014).  
976 Quantifying the impact of mechanical layering and underthrusting on the dynamics of the  
977 modern India-Asia collisional system with 3-D numerical models. *J. Geophys. Res. Solid*  
978 *Earth*, 119(1):616–644.
- 979 Li, C. and Van Der Hilst, R. D. (2010). Structure of the upper mantle and transition  
980 zone beneath Southeast Asia from traveltimes tomography. *J. Geophys. Res. Solid Earth*,  
981 115(7):1–19.
- 982 Li, S., Currie, B. S., Rowley, D. B., and Ingalls, M. (2015). Cenozoic paleoaltimetry of the  
983 SE margin of the Tibetan Plateau: Constraints on the tectonic evolution of the region.  
984 *Earth Planet. Sci. Lett.*, 432:415–424.

- 985 Li, Z., Elliott, J. R., Feng, W., Jackson, J. A., Parsons, B. E., and Walters, R. J. (2011).  
986 The 2010 Mw 6.8 Yushu (Qinghai, China) earthquake: Constraints provided by InSAR  
987 and body wave seismology. *J. Geophys. Res. Solid Earth*, 116:B10302.
- 988 Licht, A., Botsyun, S., Littell, V., Sepulchre, P., Donnadiou, Y., Risi, C., Rugenstein, J.  
989 K. C., Page, M., Huntington, K. W., and Nivet, G. D. (2019). Is Tibetan Plateau uplift  
990 more recent than we thought? In *AGU Fall Meet. Abstr.*
- 991 Licht, A., van Cappelle, M., Abels, H. A., Ladant, J.-B., Trabucho-Alexandre, J., France-  
992 Lanord, C., Donnadiou, Y., Vandenberghe, J., Rigaudier, T., Lécuyer, C., Terry Jr, D.,  
993 Adriaens, R., Boura, A., Guo, Z., Soe, A. N., Quade, J., Dupont-Nivet, G., and Jaeger,  
994 J.-J. (2014). Asian monsoons in a late Eocene greenhouse world. *Nature*, 513(7519):501–  
995 506.
- 996 Liu, Q. Y., van der Hilst, R. D., Li, Y., Yao, H. J., Chen, J. H., Guo, B., Qi, S. H., Wang,  
997 J., Huang, H., and Li, S. C. (2014). Eastward expansion of the Tibetan Plateau by crustal  
998 flow and strain partitioning across faults. *Nat. Geosci.*, 7:361–365.
- 999 Liu-Zeng, J., Tapponnier, P., Gaudemer, Y., and Ding, L. (2008). Quantifying landscape  
1000 differences across the Tibetan plateau: Implications for topographic relief evolution. *J.*  
1001 *Geophys. Res. Earth Surf.*, 113:F04018.
- 1002 Liu-Zeng, J., Zhang, J., McPhillips, D., Reiners, P., Wang, W., Pik, R., Zeng, L., Hoke, G.,  
1003 Xie, K., Xiao, P., Zheng, D., and Ge, Y. (2018). Multiple episodes of fast exhumation since  
1004 Cretaceous in southeast Tibet, revealed by low-temperature thermochronology. *Earth*  
1005 *Planet. Sci. Lett.*, 490:62–76.
- 1006 Maurin, T., Masson, F., Rangin, C., Min, U. T., and Collard, P. (2010). First global  
1007 positioning system results in northern Myanmar: Constant and localized slip rate along  
1008 the Sagaing fault. *Geology*, 38(7):591–594.

- 1009 McGroder, M. F., Lease, R. O., and Pearson, D. M. (2014). Along-strike variation in struc-  
1010 tural styles and hydrocarbon occurrences, Subandean fold-and-thrust belt and inner fore-  
1011 land, Colombia to Argentina. In *Geol. Soc. Am. Mem.*, volume 212, pages 79–113.
- 1012 McKenzie, D., Jackson, J., and Priestley, K. (2005). Thermal structure of oceanic and  
1013 continental lithosphere. *Earth Planet. Sci. Lett.*, 233:337–349.
- 1014 McKenzie, D., McKenzie, J., and Fairhead, D. (2019). The Mechanical Structure of Tibet.  
1015 *Geophys. J. Int.*, pages 950–969.
- 1016 McKenzie, D., Nimmo, F., Jackson, J. A., Gans, P. B., and Miller, E. L. (2000). Char-  
1017 acteristics and consequences of flow in the lower crust. *J. Geophys. Res. Solid Earth*,  
1018 105(B5):11029–11046.
- 1019 McKenzie, D. and Priestley, K. (2008). The influence of lithospheric thickness variations on  
1020 continental evolution. *Lithos*, 102:1–11.
- 1021 Medvedev, S. E. and Podladchikov, Y. Y. (1999a). New extended thin-sheet approximation  
1022 for geodynamic applications–I. Model formation. *Geophys. J. Int.*, 136(3):586–608.
- 1023 Medvedev, S. E. and Podladchikov, Y. Y. (1999b). New extended thin-sheet approximation  
1024 for geodynamic applications-II. Two-dimensional examples. *Geophys. J. Int.*, 136(3):586–  
1025 608.
- 1026 Merle, O. and Guillier, B. (1989). The building of the Central Swiss Alps: an experimental  
1027 approach. *Tectonophysics*, 165(1-4):41–56.
- 1028 Miller, K. G., Fairbanks, R. G., and Mountain, G. S. (1987). Tertiary Oxygen Isotope  
1029 Synthesis, Sea Level History, and Continental Margin Erosion. *Paleoceanography*, 2(1):1–  
1030 19.
- 1031 Molnar, P. and Tapponnier, P. (1978). Active Tectonics of Tibet. *J. Geophys. Res.*, 83(B11).

- 1032 Nissen, E., Tatar, M., Jackson, J., and Allen, M. (2011). New views on earthquake faulting  
1033 in the Zagros fold-and-thrust belt of Iran. *Geophys. J. Int.*, 186:928–944.
- 1034 Pattyn, F. (2003). A new three-dimensional higher-order thermomechanical ice sheet model:  
1035 Basic sensitivity, ice stream development, and ice flow across subglacial lakes. *J. Geophys.*  
1036 *Res.*, 108(B8):1–15.
- 1037 Pusok, A. E. and Kaus, B. J. P. (2015). Development of topography in 3-D continental-  
1038 collision models. *Geochemistry, Geophys. Geosystems*, 16(5):1378–1400.
- 1039 Ramberg, H. (1981). The role of gravity in orogenic belts. *Geol. Soc. Spec. Publ.*, 9:125–140.
- 1040 Reynolds, K., Copley, A., and Hussain, E. (2015). Evolution and dynamics of a fold-thrust  
1041 belt: The Sulaiman Range of Pakistan. *Geophys. J. Int.*, 201:683–710.
- 1042 Richardson, N. J., Densmore, A. L., Seward, D., Fowler, A., Wipf, M., Ellis, M. A., Yong,  
1043 L., and Zhang, Y. (2008). Extraordinary denudation in the Sichuan Basin: Insights from  
1044 low-temperature thermochronology adjacent to the eastern margin of the Tibetan Plateau.  
1045 *J. Geophys. Res. Solid Earth*, 113:B04409.
- 1046 Rowley, D. B. and Currie, B. S. (2006). Palaeo-altimetry of the late Eocene to Miocene  
1047 Lunpola basin, central Tibet. *Nature*, 439:677–681.
- 1048 Rowley, D. B., Pierrehumbert, R. T., and Currie, B. S. (2001). A new approach to stable  
1049 isotope-based paleoaltimetry: Implications for paleoaltimetry and paleohypsometry of the  
1050 High Himalaya since the late Miocene. *Earth Planet. Sci. Lett.*, 188:253–268.
- 1051 Royden, L. H., Burchfiel, B. C., King, R. W., Wang, E., Chen, Z., Shen, F., and Liu, Y.  
1052 (1997). Surface Deformation and Lower Crustal Flow in Eastern Tibet. *Science (80-. )*,  
1053 276(5313):788–790.

- 1054 Rybacki, E., Gottschalk, M., Wirth, R., and Dresen, G. (2006). Influence of water fugacity  
1055 and activation volume on the flow properties of fine-grained anorthite aggregates. *J.*  
1056 *Geophys. Res. Solid Earth*, 111(3).
- 1057 Saad, Y. and Schultz, M. H. (1986). GMRES: A Generalized Minimal Residual Algorithm  
1058 for Solving Nonsymmetric Linear Systems. *SIAM J. Sci. Stat. Comput.*, 7(3):856–869.
- 1059 Savin, S. M. (1977). The History of the Earth’s Surface Temperature During the Past 100  
1060 Million Years. *Annu. Rev. Earth Planet. Sci.*, 5(1):319–355.
- 1061 Schmalholz, S. M., Medvedev, S., Lechmann, S. M., and Podladchikov, Y. (2014). Relation-  
1062 ship between tectonic overpressure, deviatoric stress, driving force, isostasy and gravita-  
1063 tional potential energy. *Geophys. J. Int.*, 197(2):680–696.
- 1064 Shen, Z. K., Lü, J., Wang, M., and Bürgmann, R. (2005). Contemporary crustal deformation  
1065 around the southeast borderland of the Tibetan Plateau. *J. Geophys. Res. Solid Earth*,  
1066 110:B11409.
- 1067 Sonder, L. J. and England, P. (1986). Vertical averages of rheology of the continental  
1068 lithosphere: relation to thin sheet parameters. *Earth Planet. Sci. Lett.*, 77:81–90.
- 1069 Steckler, M. S., Mondal, D. R., Akhter, S. H., Seeber, L., Feng, L., Gale, J., Hill, E. M., and  
1070 Howe, M. (2016). Locked and loading megathrust linked to active subduction beneath the  
1071 Indo-Burman Ranges. *Nat. Geosci.*, 9:615–618.
- 1072 Stocker, R. L. and Ashby, M. F. (1973). On the rheology of the upper mantle. *Rev. Geophys.*,  
1073 11(2):391–426.
- 1074 Stork, A. L., Selby, N. D., Heyburn, R., and Searle, M. P. (2008). Accurate relative earth-  
1075 quake hypocenters reveal structure of the Burma subduction zone. *Bull. Seismol. Soc.*  
1076 *Am.*, 98(6):2815–2827.

- 1077 Tang, M., Liu-Zeng, J., Hoke, G. D., Xu, Q., Wang, W., Li, Z., Zhang, J., and Wang, W.  
1078 (2017). Paleoelevation reconstruction of the Paleocene-Eocene Gonjo basin, SE-central  
1079 Tibet. *Tectonophysics*, 712-713:170–181.
- 1080 Turcotte, D. and Schubert, G. (2014). Body Forces and Surface Forces. In *Geodynamics*,  
1081 chapter 2, pages 93–98. Cambridge University Press, 3rd edition.
- 1082 Vilotte, J. P., Daignieres, M., Madariaga, R., and Zienkiewicz, O. C. (1984). The role of a  
1083 heterogeneous inclusion during continental collision. *Phys. Earth Planet. Inter.*, 36:236–  
1084 259.
- 1085 Wang, E. and Burchfiel, B. C. (1997). Interpretation of Cenozoic Tectonics in the Right-  
1086 Lateral Accommodation Zone Between the Ailao Shan Shear Zone and the Eastern Hi-  
1087 malayan Syntaxis. *Int. Geol. Rev.*, 39(3):191–219.
- 1088 Wang, E., Kirby, E., Furlong, K. P., Van Soest, M., Xu, G., Shi, X., Kamp, P. J. J., and  
1089 Hodges, K. V. (2012). Two-phase growth of high topography in eastern Tibet during the  
1090 Cenozoic. *Nat. Geosci.*, 5:640–645.
- 1091 Wang, Y., Sieh, K., Tun, S. T., Lai, K.-Y., and Myint, T. (2014). Active tectonics and  
1092 earthquake potential of the Myanmar region. *J. Geophys. Res. Solid Earth*, 119:3767–  
1093 3822.
- 1094 Wang, Y., Zhang, B., Schoenbohm, L. M., Zhang, J., Zhou, R., Hou, J., and Ai, S. (2016).  
1095 Late Cenozoic tectonic evolution of the Ailao Shan-Red River fault (SE Tibet): Implica-  
1096 tions for kinematic change during plateau growth. *Tectonics*, 35:1969–1988.
- 1097 Wessel, P., Smith, W. H. F., Scharroo, R., Luis, J., and Wobbe, F. (2013). Generic Mapping  
1098 Tools: Improved version released. *EOS Trans. AGU*, 94(45):409–410.

- 1099 Wittlinger, G., Vergne, J., Tapponnier, P., Farra, V., Poupinet, G., Jiang, M., Su, H.,  
1100 Herquel, G., and Paul, A. (2004). Teleseismic imaging of subducting lithosphere and  
1101 Moho offsets beneath western Tibet. *Earth Planet. Sci. Lett.*, 221(1-4):117–130.
- 1102 Wu, J., Zhang, K., Xu, Y., Wang, G., Garzzone, C. N., Eiler, J., Leloup, P. H., Sorrel, P.,  
1103 and Mahéo, G. (2018). Paleoelevations in the Jianchuan Basin of the southeastern Tibetan  
1104 Plateau based on stable isotope and pollen grain analyses. *Palaeogeogr. Palaeoclimatol.*  
1105 *Palaeoecol.*, 510(March):93–108.
- 1106 Xu, Q., Liu, X., and Ding, L. (2016). Miocene high-elevation landscape of the eastern  
1107 Tibetan Plateau. *Geochemistry, Geophys. Geosystems*, 17(10):4254–4267.
- 1108 Yang, R., Willett, S. D., and Goren, L. (2015). In situ low-relief landscape formation as a  
1109 result of river network disruption. *Nature*, 520:526–529.
- 1110 Zachos, J., Pagani, H., Sloan, L., Thomas, E., and Billups, K. (2001). Trends, rhythms, and  
1111 aberrations in global climate 65 Ma to present. *Science (80-. )*, 292(5517):686–693.
- 1112 Zhang, P.-Z., Wen, X.-Z., Shen, Z.-K., and Chen, J.-H. (2010). Oblique, High-Angle, Listric-  
1113 Reverse Faulting and Associated Development of Strain: The Wenchuan Earthquake of  
1114 May 12, 2008, Sichuan, China. *Annu. Rev. Earth Planet. Sci.*, 38(1):353–382.
- 1115 Zheng, G., Wang, H., Wright, T. J., Lou, Y., Zhang, R., Zhang, W., Shi, C., Huang, J., and  
1116 Wei, N. (2017). Crustal Deformation in the India-Eurasia Collision Zone From 25 Years  
1117 of GPS Measurements. *J. Geophys. Res. Solid Earth*, 122(11):9290–9312.

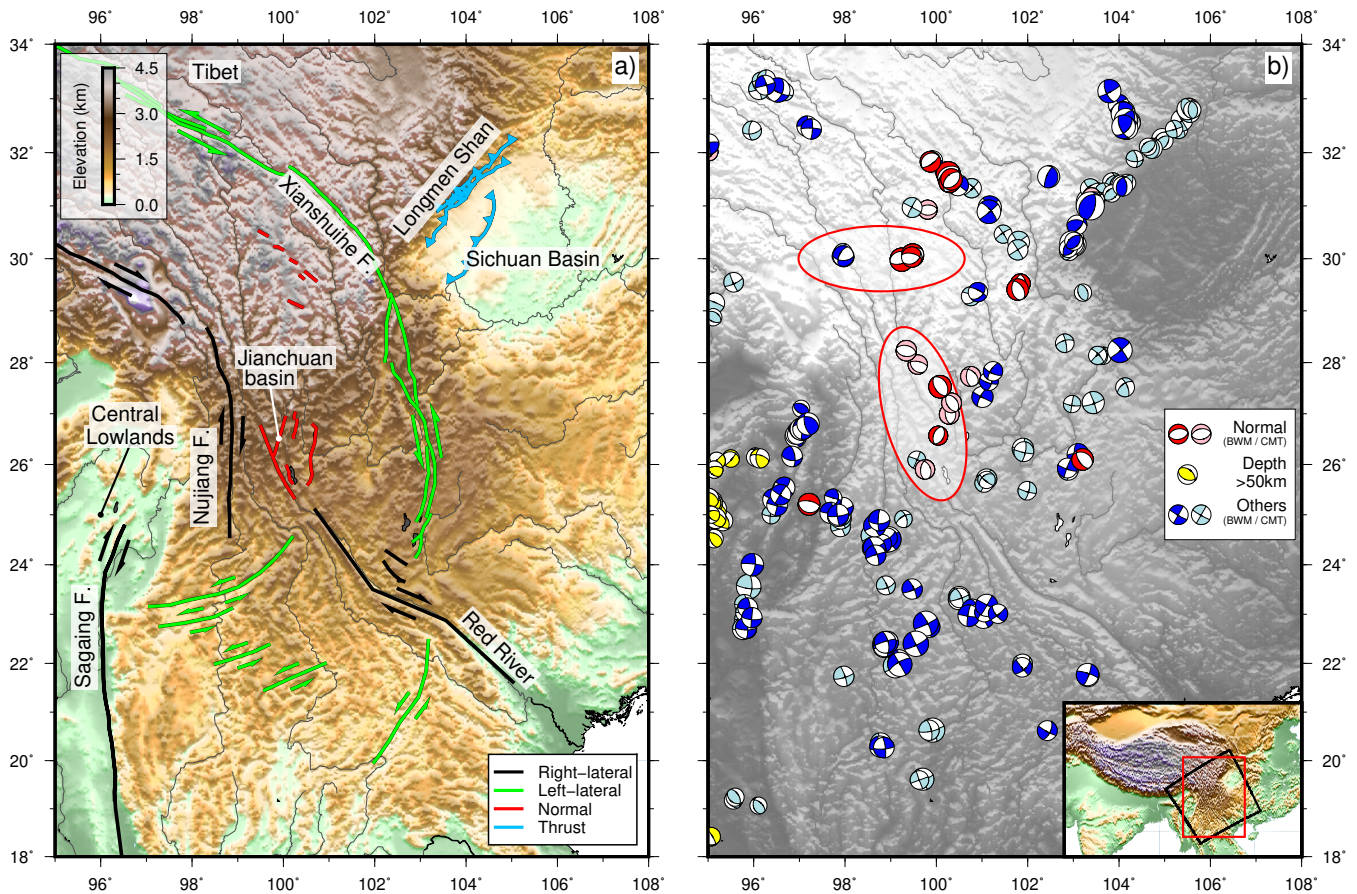


Figure 1: a) Major active faults in south-east Tibet, from Copley (2008); Hubbard and Shaw (2009). Black and green lines are right- and left-lateral strike-slip faults respectively. Note the opposite sense of shear adjacent to the Central Lowlands of Myanmar and Sichuan Basin. Red lines show normal faults. Blue lines show thrust faults with teeth on the hanging-wall side. b) Focal mechanisms of earthquakes in south-east Tibet. Focal mechanisms determined from body-waveform modelling from Copley (2008) (and references therein), Zhang et al. (2010), Li et al. (2011), Han et al. (2014), Bai et al. (2017), Han et al. (2018) are shown in red if they have a rake of  $-90 \pm 35^\circ$  (normal faulting), and dark blue otherwise. Yellow focal mechanisms are  $>50$  km deep and are associated with subduction beneath the Indo-Burman ranges, all other earthquakes have depths less than  $\sim 20$  km. Focal mechanisms in pink (normal faulting, with rakes of  $-90 \pm 35^\circ$ ) and pale blue are those from the CMT catalogue with  $>70\%$  double couple and  $>10$  depth phases in the EHB catalogue if the earthquake occurred before 2009. Two regions of normal faulting discussed in the text are circled in red. Red box in inset shows the figure's location, black box shows location of Figure 3.

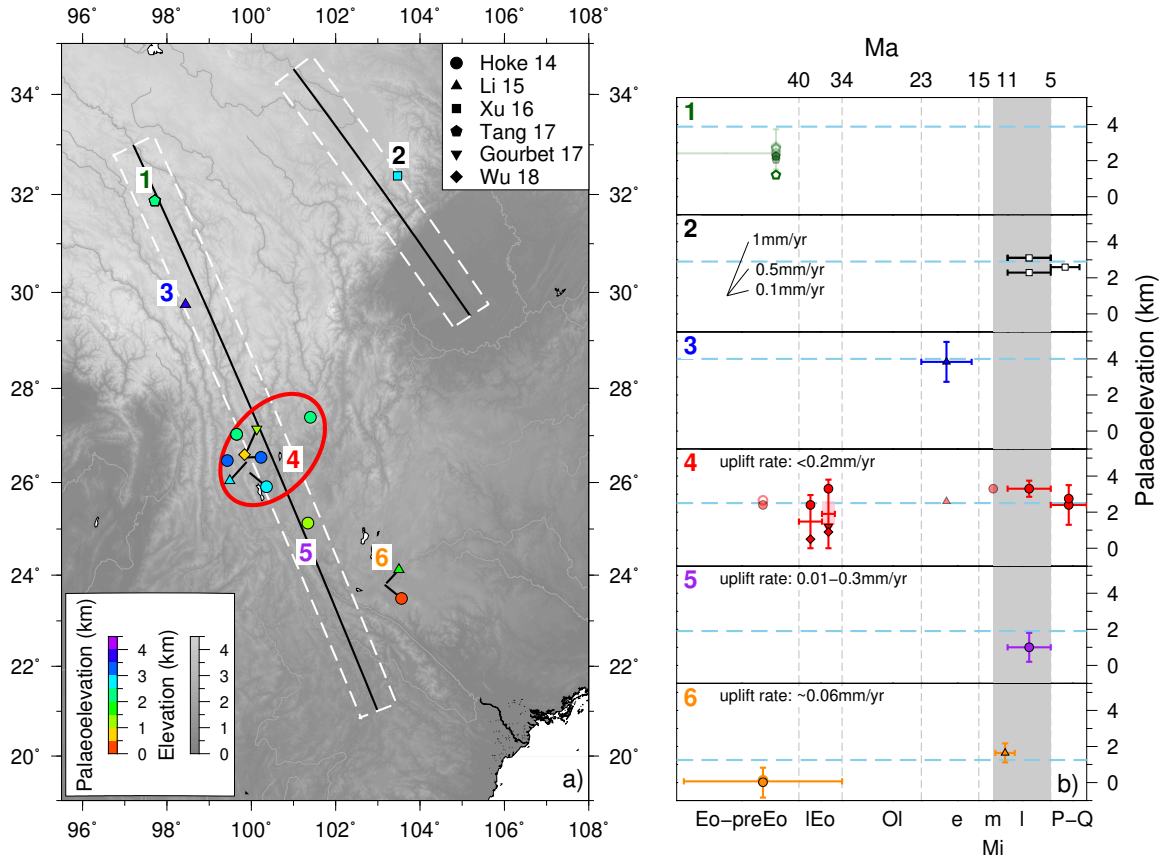


Figure 2: Results of stable-isotope palaeoaltimetry studies in south-east Tibet. a) Sample localities from Hoke et al. (2014); Li et al. (2015); Xu et al. (2016); Tang et al. (2017); Gourbet et al. (2017) and Wu et al. (2018) are coloured by palaeoelevation. 6 regions are labelled, which correspond to panels in b, the red ellipse indicates the extent of region 4. Black lines with white boxes show the regions plotted as topographic profiles in Figure 6g and h. b) Sample ages and palaeoelevations in each region. Epoch labels are – Eo-preEo: Eocene-pre Eocene >40 Ma, lEo: late Eocene: 40–34 Ma, Ol: Oligocene 34–23 Ma, eMi: early Miocene 23–15 Ma, mMi: middle Miocene 15–11 Ma, lMi: late Miocene 7–5 Ma, P-Q: Pliocene–Quaternary 5–0 Ma. Where multiple samples from the same author are reported in the same epoch in the same region only a single error bar (representing the highest and lowest palaeoelevation estimates) is plotted. Palaeoelevation estimates using a modern temperature-elevation relationship are shown as filled symbols, those using a higher Eocene temperature estimate are unfilled. The colour of symbols corresponds to their region in a). Pale-outlined points in regions 1 and 4 are the authors’ original palaeoelevation/age inferences. Dark-outlined points show the revised palaeoelevations/ages from Gourbet et al. (2017) and Wu et al. (2018), which we use to determine uplift rates. In region 4 the pink rectangle corresponds to the range of palaeoelevation estimates derived from palynology by Wu et al. (2018). Symbol shapes are as in a). Grey bar shows the timing of increased exhumation and erosion rates suggested by Clark et al. (2005b) to indicate rapid uplift. Dashed blue lines indicate mean present-day sample-site elevation for each region.

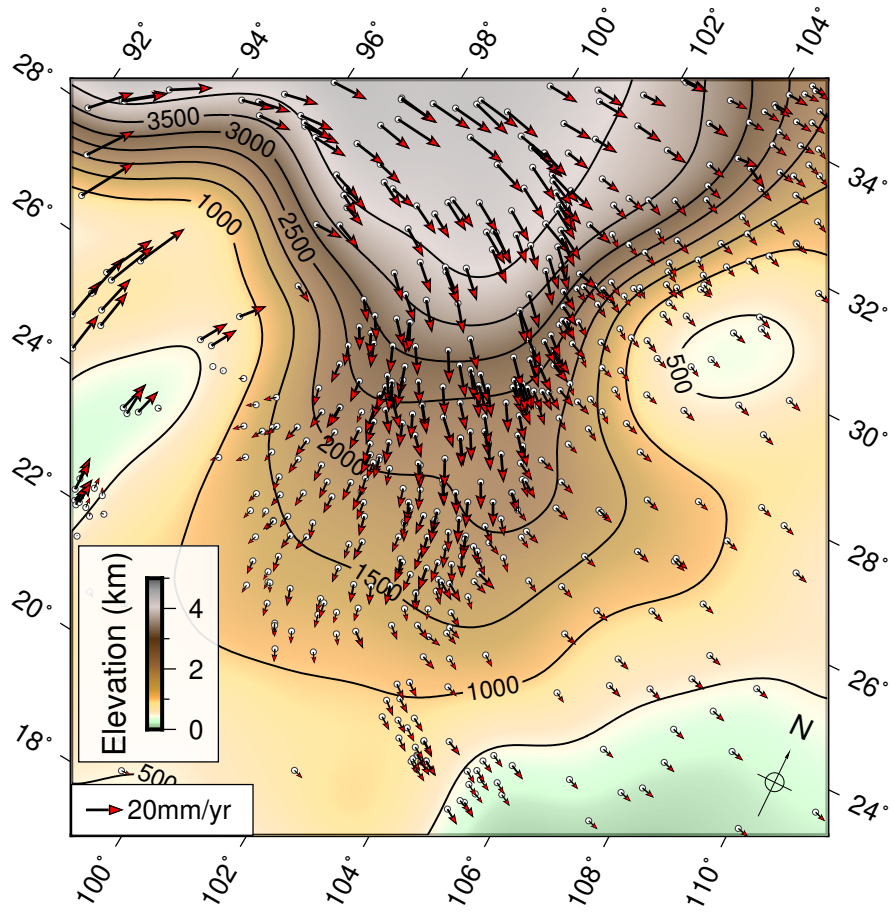


Figure 3: Topography of south-east Tibet after applying a low-pass 500 km-diameter Gaussian filter in an oblique Mercator projection (equator azimuth 60°, centred on 101.5° E, 26.5° N, location shown as black box in the inset of Figure 1b) for comparison to our model set-up (Figure 4) and results (Figures 5 and 8, Section 4). GPS velocities from Zheng et al. (2017) are shown in a Eurasia-fixed reference frame.

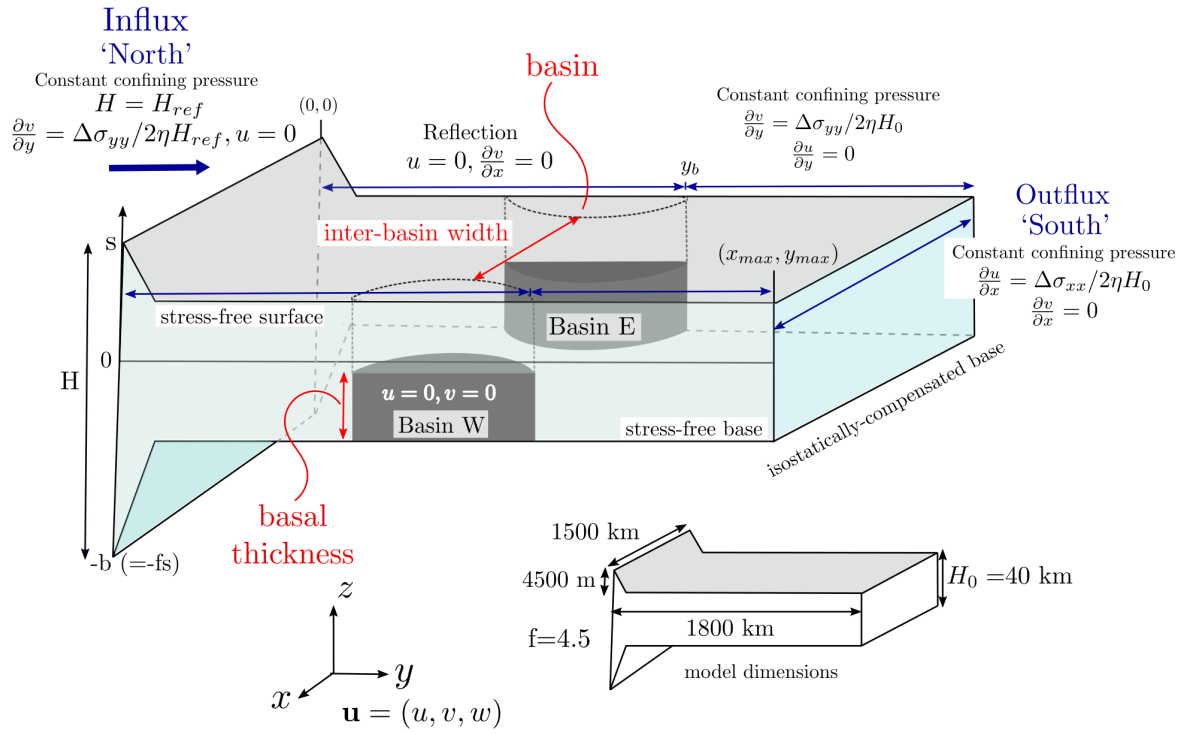


Figure 4: Model geometry, showing the initial topography and symmetric rigid regions. Boundary conditions on  $x = x_{max}$  are the same as those on  $x = 0$ . Inset shows dimensions of model domain. The isostatic root is not shown to scale.

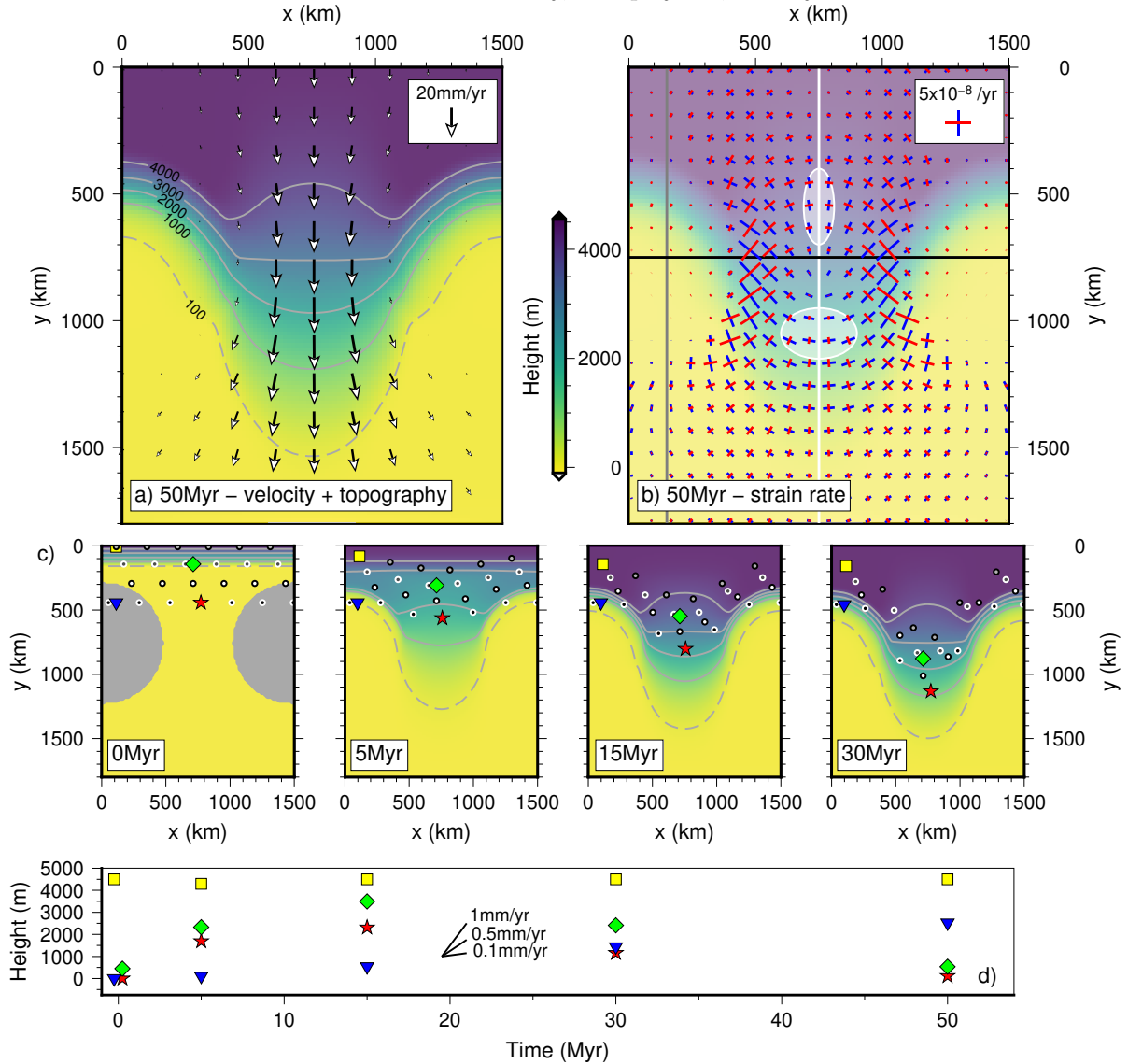


Figure 5: Modelling results for a symmetric model (both basins have the same size and location in  $y$ ) with 450 km-radius basins (grey semicircles at 0 Myr in c) with a 15 km-thick rigid base. The influx boundary (left-hand side in Figure 4) is at the top of each panel. a) topography and velocities after 50 Myr for a fluid with a viscosity of  $10^{22}$  Pas. Topography is plotted relative to the surface of 40 km-thick, isostatically-compensated crust and contoured at 100 m (dashed line), 1000 m, 2000 m, 3000 m and 4000 m. b) principal axes of the surface horizontal strain-rate tensor after 50 Myr. Blue bars are extensional, red bars are compressional. Gray, white and black lines show locations of profiles in Figures 6c, d and 7c respectively. White ellipses show the two regions where extensional strain rates are  $\sim 2$ – $5$  times greater than compressional strain rates, discussed in Section 5. c) Evolution of topography through time. Dots show large-scale lateral transport of particles moving with the surface of the current and can be viewed as analogous to the motion of near-surface carbonates used for palaeoaltimetry (Section 3.2). Contours are at 100 m (dashed line), 1000 m, 2000 m, 3000 m and 4000 m. d) shows the elevation history of the shaped particles in c. Since the particles are advected with the current their elevation can decrease as well as increase.

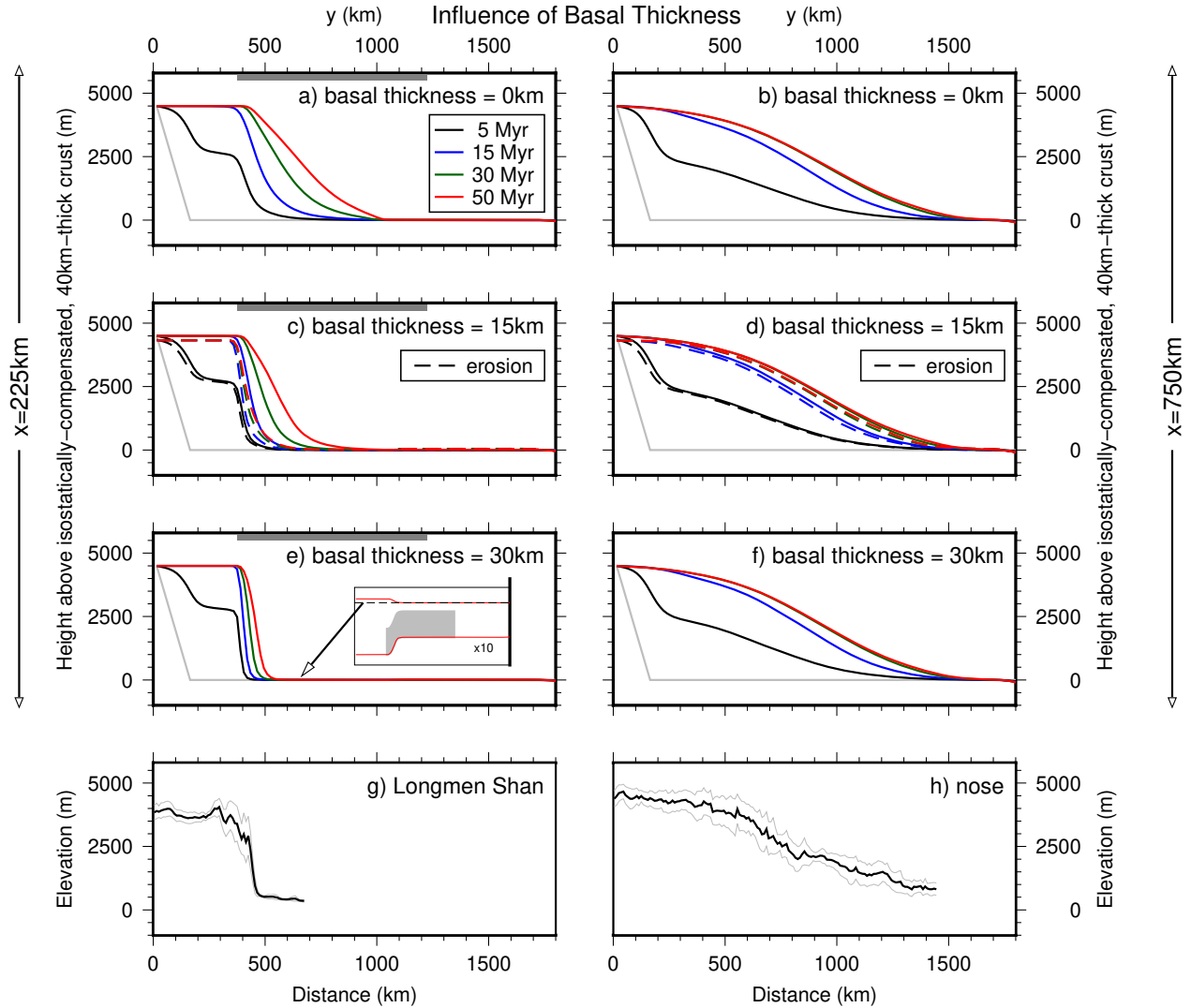


Figure 6: Effect of changing the basal thickness of the rigid basin (analogous to the thickness of undeforming lower crust) on the propagation of topography. The lateral extent of the basin which has a rigid basal thickness is indicated by the grey bars in a, c and e. a), c) and e) show profiles through the basin (gray line in Figure 5b) for basal thicknesses of 0 km (rigid base), 15 km and 30 km respectively. b), d) and f) show profiles through the inter-basin (stress-free base) region (white line in Figure 5b) for basal thicknesses of 0 km (rigid base), 15 km and 30 km respectively. The basal thickness has no significant effect on the development of topography in the regions with stress-free base. Elevations are relative to the surface of 40 km-thick, isostatically-compensated crust. Inset in e) shows the full thickness of the current (10x vertical exaggeration) to demonstrate how topography in this figure relates to full model. Grey region is the rigid basin. Dashed lines in c) and d) show the effect of erosion with  $\kappa = 4 \text{ mm yr}^{-1}$  in equation (1). c and d are profiles through the same model shown in Figure 5. g) and h) show topographic profiles and standard deviation across the Longmen Shan and between the Sichuan Basin and Central Lowlands of Myanmar respectively (profile locations shown in Figure 2a), demonstrating the similarity of topographic gradients in south-east Tibet to those resulting from our model.

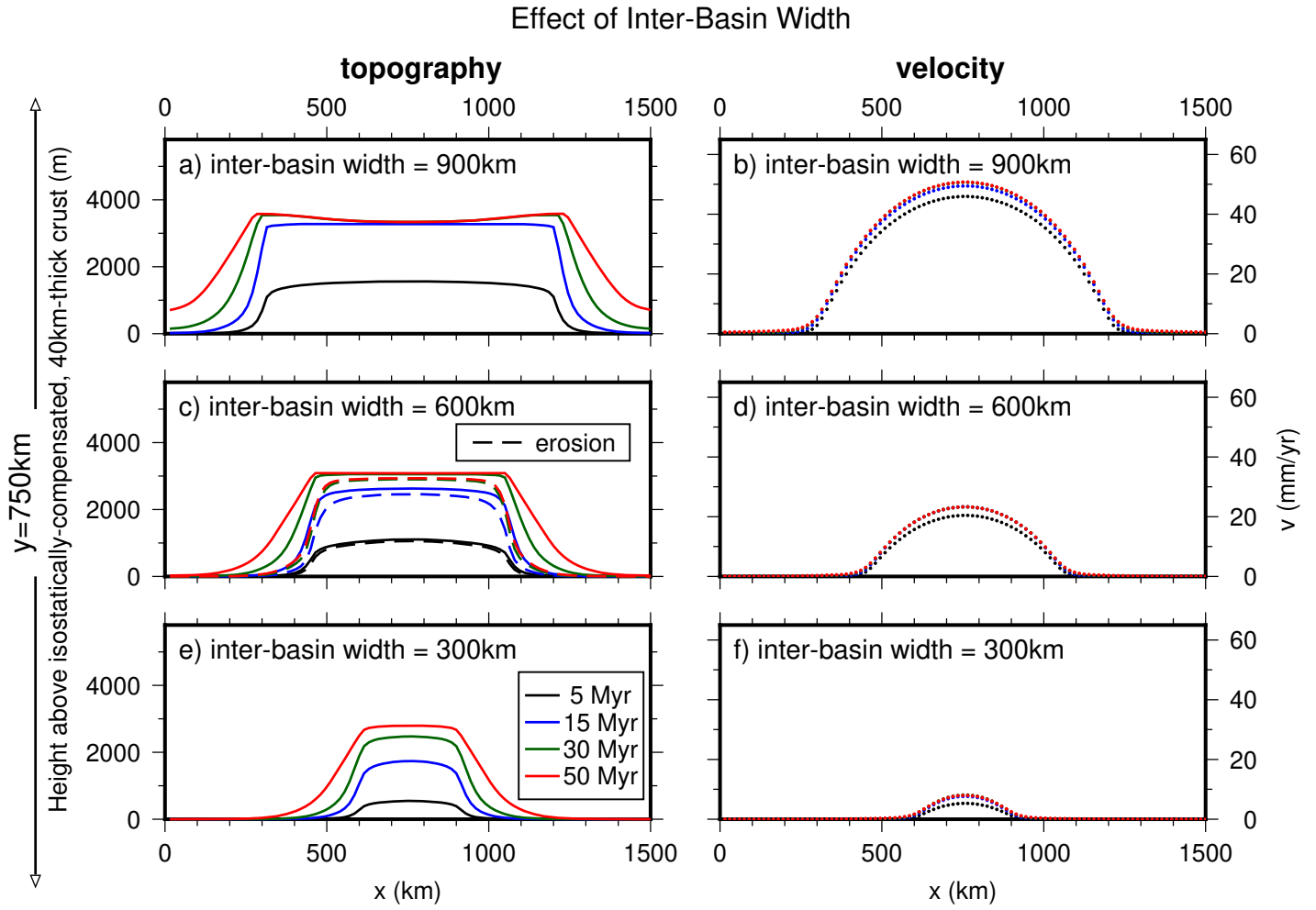


Figure 7: Effect of changing the distance between basins (inter-basin width, Figure 4). In each case profiles are taken at the centre of the semi-circular regions (black line in Figure 5b shows location of c and d), which have a basal thickness of 15 km. Elevations are relative to the surface of 40 km-thick, isostatically-compensated crust. a) and b) 900 km inter-basin width. a) shows the evolution of topography through time. The saddle arises because of thinning due to rapid velocities in the centre of the inter-basin region. b) the velocity perpendicular to the profile ( $v$  in Figure 4) after 50 Myr. c) and d) as for a and b but for an inter-basin width of 600 km. Note that c) and d) are profiles through the same model as Figure 5 and Figures 6c and d, with basin radius 450 km, inter-basin width 600 km and basal thickness 15 km. Dashed lines show the effects of erosion with  $\kappa = 4 \text{ mm yr}^{-1}$  in equation (1). e) and f) as for a and b but for an inter-basin width of 300 km.

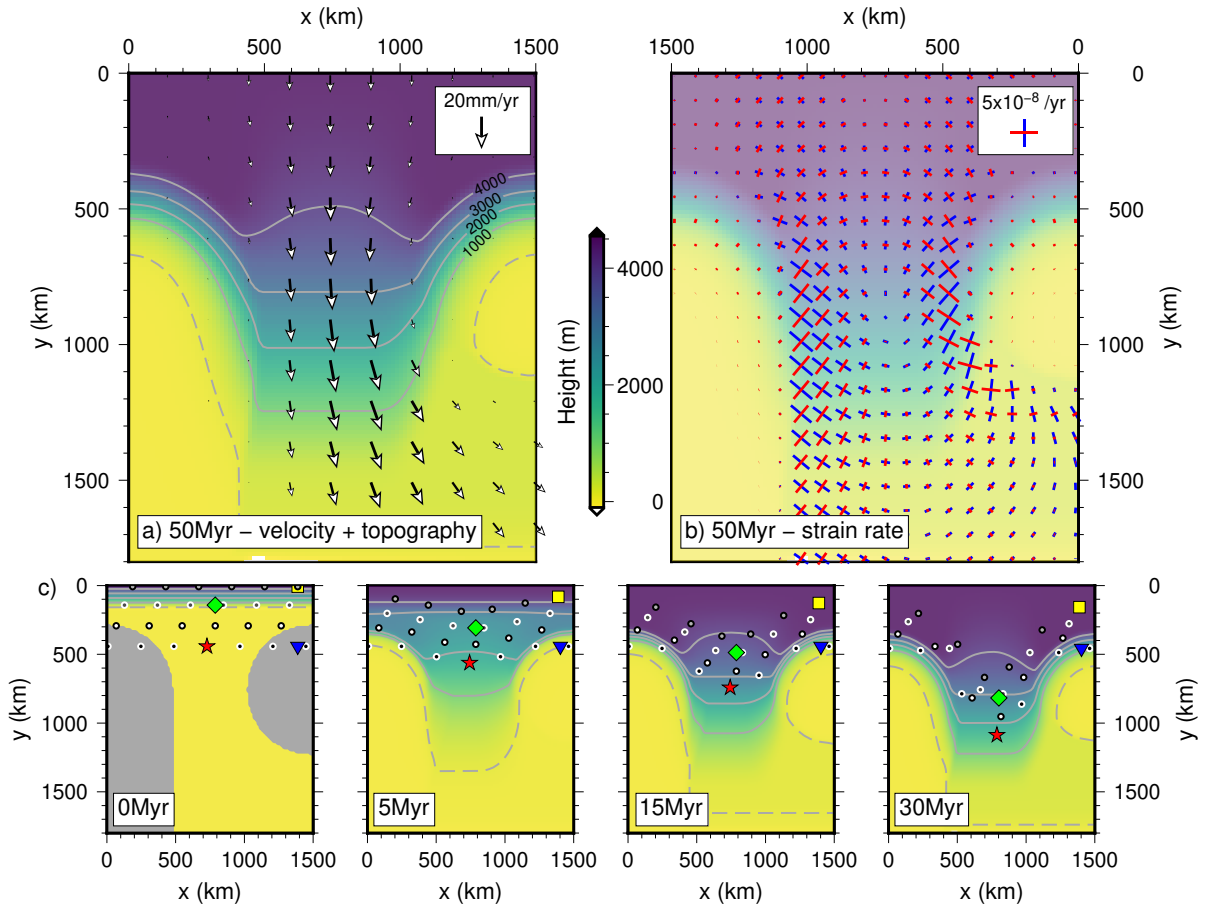


Figure 8: Modelling results for an asymmetric model set-up with 15 km basal thickness in the regions shown in grey in the 0 Myr panel of c. Panels are as for Figure 5. Note the broader region of shear adjacent to the extended basin.

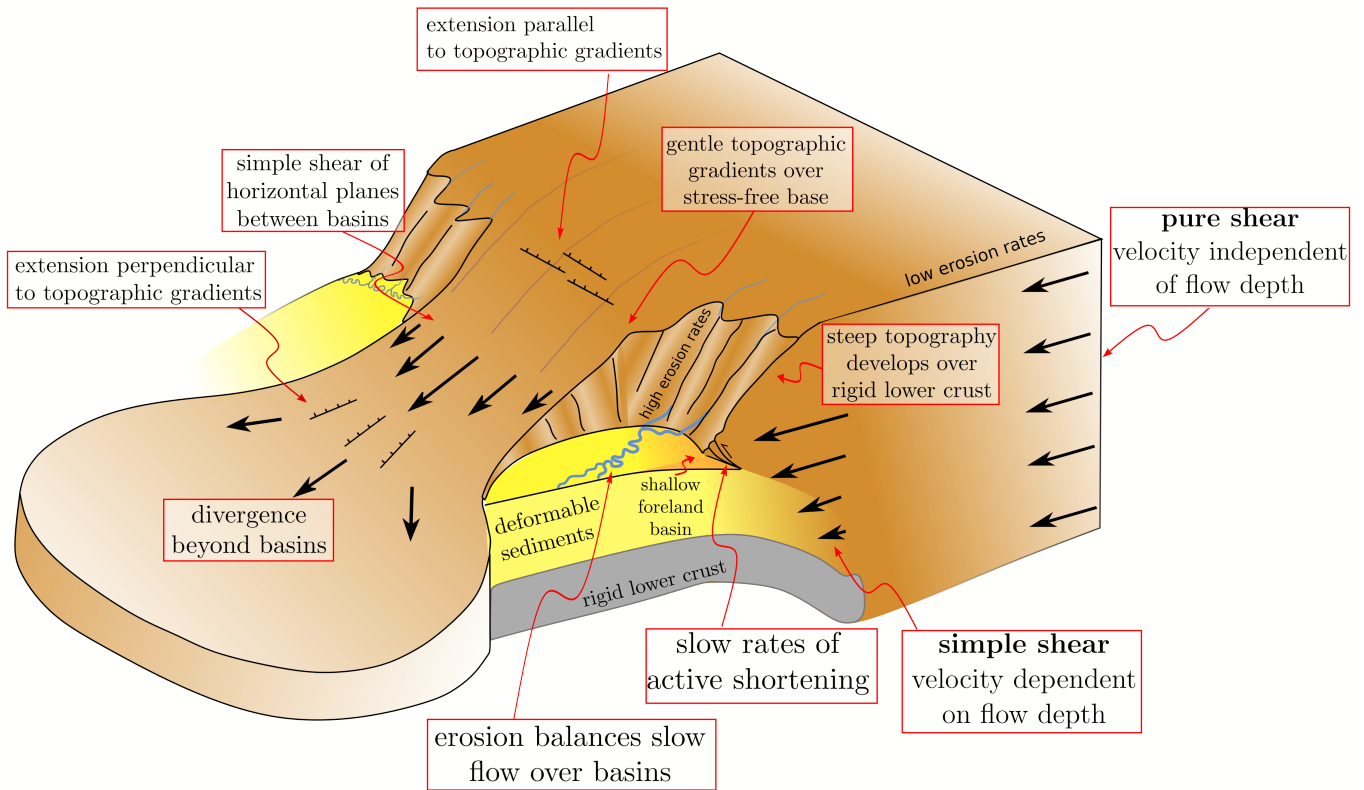


Figure 9: Cartoon showing effects of a rigid region on the development of topography. Steep topographic gradients develop above the region of rigid lower crust because of the dependence of velocity on flow depth. The compressional strain rates associated with growth of this steep topography are much less than the shear strain rates between basins. Regions with a stress-free base (without strong lower crust) deform by pure shear of vertical planes, which results in gentle topographic gradients. Between two rigid regions flow is dominated by simple shear of horizontal planes, similar to flow in a pipe. Beyond the basins the flow can spread out, leading to extension.

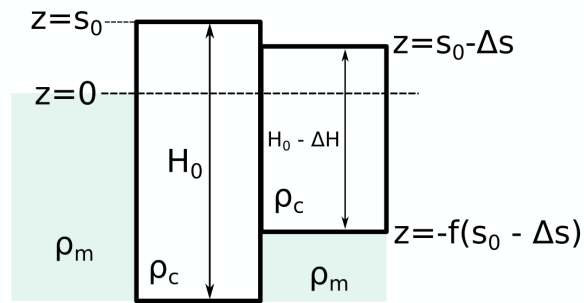


Figure A.1: Diagram to show isostatic balance used to find boundary conditions on  $x = 0, x_{max}$ . The column of mantle on the left hand side of the figure is to demonstrate that the reference level is set by a column of mantle. The deviatoric stress between the two columns of continental crust is calculated by integrating the pressure difference between them and dividing by the thickness (e.g. Artyushkov, 1973; Molnar and Tapponnier, 1978; Dalmayrac and Molnar, 1981; Turcotte and Schubert, 2014).